



First Very Long Baseline Interferometry Detections at 870 μm

Downloaded from: <https://research.chalmers.se>, 2024-11-19 04:13 UTC

Citation for the original published paper (version of record):

Raymond, A., Doeleman, S., Asada, K. et al (2024). First Very Long Baseline Interferometry Detections at 870 μm . *Astronomical Journal*, 168(3). <http://dx.doi.org/10.3847/1538-3881/ad5bdb>

N.B. When citing this work, cite the original published paper.

- George N. Wong^{42,144} , Qingwen Wu (吴庆文)¹⁴⁵ , Nitika Yadlapalli³² , Paul Yamaguchi² , Aristomenis Yfantis¹⁸ ,
 Doosoo Yoon¹⁰⁹ , Ziri Younsi^{53,146} , Wei Yu (于威)² , Feng Yuan (袁峰)¹⁴⁷ , Ye-Fei Yuan (袁业飞)¹⁴⁸ ,
 J. Anton Zensus⁹ , Shuo Zhang¹⁴⁹ , Guang-Yao Zhao^{9,21} , and Shan-Shan Zhao (赵杉杉)⁴⁶ 
- ¹ Black Hole Initiative at Harvard University, 20 Garden Street, Cambridge, MA 02138, USA; sdoeleman@cfa.harvard.edu
² Center for Astrophysics | Harvard & Smithsonian, 60 Garden Street, Cambridge, MA 02138, USA
³ Current address is Jet Propulsion Laboratory, California Institute of Technology, Pasadena, CA, USA
⁴ Institute of Astronomy and Astrophysics, Academia Sinica, 11F of Astronomy-Mathematics Building, AS/NTU No. 1, Sec. 4, Roosevelt Road, Taipei 106216, Taiwan, R.O.C.
⁵ Institute of Astronomy and Astrophysics, Academia Sinica, 645 North A'ohoku Place, Hilo, HI 96720, USA
⁶ Department of Physics and Astronomy, University of Hawaii at Manoa, 2505 Correa Road, Honolulu, HI 96822, USA
⁷ Institut de Radioastronomie Millimétrique (IRAM), 300 rue de la Piscine, F-38406 Saint Martin d'Hères, France
⁸ Massachusetts Institute of Technology Haystack Observatory, 99 Millstone Road, Westford, MA 01886, USA
⁹ Max-Planck-Institut für Radioastronomie, Auf dem Hügel 69, D-53121 Bonn, Germany
¹⁰ Dipartimento di Fisica, Università degli Studi di Cagliari, SP Monserrato-Sestu km 0.7, I-09042 Monserrato, Italy
¹¹ INAF-Osservatorio Astronomico di Cagliari, Via della Scienza 5, 09047, Selargius, CA, Italy
¹² Department of Physics, National Taiwan University, No. 1, Sec. 4, Roosevelt Road, Taipei 106216, Taiwan, R.O.C.
¹³ Astronomy Department, Universidad de Concepción, Casilla 160-C, Concepción, Chile
¹⁴ Finnish Centre for Astronomy with ESO, FI-20014 University of Turku, Finland
¹⁵ Aalto University Metsähovi Radio Observatory, Metsähovintie 114, FI-02540 Kylmälahti, Finland
¹⁶ Institut de Radioastronomie Millimétrique (IRAM), Avenida Divina Pastora 7, Local 20, E-18012, Granada, Spain
¹⁷ Steward Observatory and Department of Astronomy, University of Arizona, 933 North Cherry Avenue, Tucson, AZ 85721, USA
¹⁸ Department of Astrophysics, Institute for Mathematics, Astrophysics and Particle Physics (IMAPP), Radboud University, P.O. Box 9010, 6500 GL Nijmegen, The Netherlands
¹⁹ National Astronomical Observatory of Japan, 2-21-1 Osawa, Mitaka, Tokyo 181-8588, Japan
²⁰ Departament d'Astronomia i Astrofísica, Universitat de València, C. Dr. Moliner 50, E-46100 Burjassot, València, Spain
²¹ Instituto de Astrofísica de Andalucía-CSIC, Glorieta de la Astronomía s/n, E-18008 Granada, Spain
²² Department of Physics, Faculty of Science, Universiti Malaya, 50603 Kuala Lumpur, Malaysia
²³ Department of Physics & Astronomy, The University of Texas at San Antonio, One UTSA Circle, San Antonio, TX 78249, USA
²⁴ Observatori Astronòmic, Universitat de València, C. Catedrático José Beltrán 2, E-46980 Paterna, València, Spain
²⁵ Department of Space, Earth and Environment, Chalmers University of Technology, Onsala Space Observatory, SE-43992 Onsala, Sweden
²⁶ Yale Center for Astronomy & Astrophysics, Yale University, 52 Hillhouse Avenue, New Haven, CT 06511, USA
²⁷ Department of Physics, University of Illinois, 1110 West Green Street, Urbana, IL 61801, USA
²⁸ Fermi National Accelerator Laboratory, MS209, P.O. Box 500, Batavia, IL 60510, USA
²⁹ Department of Astronomy and Astrophysics, University of Chicago, 5640 South Ellis Avenue, Chicago, IL 60637, USA
³⁰ East Asian Observatory, 660 North A'ohoku Place, Hilo, HI 96720, USA
³¹ James Clerk Maxwell Telescope (JCMT), 660 North A'ohoku Place, Hilo, HI 96720, USA
³² California Institute of Technology, 1200 East California Boulevard, Pasadena, CA 91125, USA
³³ Department of Physics, McGill University, 3600 rue University, Montréal, QC H3A 2T8, Canada
³⁴ Trottier Space Institute at McGill, 3550 rue University, Montréal, QC H3A 2A7, Canada
³⁵ Perimeter Institute for Theoretical Physics, 31 Caroline Street North, Waterloo, ON N2L 2Y5, Canada
³⁶ Department of Physics and Astronomy, University of Waterloo, 200 University Avenue West, Waterloo, ON N2L 3G1, Canada
³⁷ Waterloo Centre for Astrophysics, University of Waterloo, Waterloo, ON N2L 3G1, Canada
³⁸ Department of Astronomy, University of Massachusetts, Amherst, MA 01003, USA
³⁹ Kavli Institute for Cosmological Physics, University of Chicago, 5640 South Ellis Avenue, Chicago, IL 60637, USA
⁴⁰ Department of Physics, University of Chicago, 5720 South Ellis Avenue, Chicago, IL 60637, USA
⁴¹ Enrico Fermi Institute, University of Chicago, 5640 South Ellis Avenue, Chicago, IL 60637, USA
⁴² Princeton Gravity Initiative, Jadwin Hall, Princeton University, Princeton, NJ 08544, USA
⁴³ Data Science Institute, University of Arizona, 1230 North Cherry Avenue, Tucson, AZ 85721, USA
⁴⁴ Program in Applied Mathematics, University of Arizona, 617 North Santa Rita, Tucson, AZ 85721, USA
⁴⁵ Cornell Center for Astrophysics and Planetary Science, Cornell University, Ithaca, NY 14853, USA
⁴⁶ Shanghai Astronomical Observatory, Chinese Academy of Sciences, 80 Nandan Road, Shanghai 200030, People's Republic of China
⁴⁷ Key Laboratory of Radio Astronomy and Technology, Chinese Academy of Sciences, A20 Datun Road, Chaoyang District, Beijing, 100101, People's Republic of China
⁴⁸ Korea Astronomy and Space Science Institute, Daedeok-daero 776, Yuseong-gu, Daejeon 34055, Republic of Korea
⁴⁹ Department of Astronomy, Yonsei University, Yonsei-ro 50, Seodaemun-gu, 03722 Seoul, Republic of Korea
⁵⁰ Physics Department, Fairfield University, 1073 North Benson Road, Fairfield, CT 06824, USA
⁵¹ Department of Astronomy, University of Illinois at Urbana-Champaign, 1002 West Green Street, Urbana, IL 61801, USA
⁵² Instituto de Astronomía, Universidad Nacional Autónoma de México (UNAM), Apdo Postal 70-264, Ciudad de México, Mexico
⁵³ Institut für Theoretische Physik, Goethe-Universität Frankfurt, Max-von-Laue-Straße 1, D-60438 Frankfurt am Main, Germany
⁵⁴ Research Center for Astronomical Computing, Zhejiang Laboratory, Hangzhou 311100, People's Republic of China
⁵⁵ Tsung-Dao Lee Institute, Shanghai Jiao Tong University, Shengrong Road 520, Shanghai, 201210, People's Republic of China
⁵⁶ Department of Astronomy and Columbia Astrophysics Laboratory, Columbia University, 500 West 120th Street, New York, NY 10027, USA
⁵⁷ Center for Computational Astrophysics, Flatiron Institute, 162 Fifth Avenue, New York, NY 10010, USA
⁵⁸ Dipartimento di Fisica "E. Pancini", Università di Napoli "Federico II", Compl. Univ. di Monte S. Angelo, Edificio G, Via Cinthia, I-80126, Napoli, Italy
⁵⁹ INFN Sez. di Napoli, Compl. Univ. di Monte S. Angelo, Edificio G, Via Cinthia, I-80126, Napoli, Italy
⁶⁰ Wits Centre for Astrophysics, University of the Witwatersrand, 1 Jan Smuts Avenue, Braamfontein, Johannesburg 2050, South Africa
⁶¹ Department of Physics, University of Pretoria, Hatfield, Pretoria 0028, South Africa
⁶² Centre for Radio Astronomy Techniques and Technologies, Department of Physics and Electronics, Rhodes University, Makhanda 6140, South Africa
⁶³ ASTRON, Oude Hoogeveensedijk 4, 7991 PD Dwingeloo, The Netherlands
⁶⁴ LESIA, Observatoire de Paris, Université PSL, CNRS, Sorbonne Université, Université de Paris, 5 place Jules Janssen, F-92195 Meudon, France
⁶⁵ JILA and Department of Astrophysical and Planetary Sciences, University of Colorado, Boulder, CO 80309, USA
⁶⁶ National Astronomical Observatories, Chinese Academy of Sciences, 20A Datun Road, Chaoyang District, Beijing 100101, People's Republic of China
⁶⁷ Las Cumbres Observatory, 6740 Cortona Drive, Suite 102, Goleta, CA 93117-5575, USA
⁶⁸ Department of Physics, University of California, Santa Barbara, CA 93106-9530, USA
⁶⁹ National Radio Astronomy Observatory, 520 Edgemont Road, Charlottesville, VA 22903, USA

- ⁷⁰ Department of Electrical Engineering and Computer Science, Massachusetts Institute of Technology, 32-D476, 77 Massachusetts Avenue, Cambridge, MA 02142, USA
- ⁷¹ Google Research, 355 Main Street, Cambridge, MA 02142, USA
- ⁷² Institut für Theoretische Physik und Astrophysik, Universität Würzburg, Emil-Fischer-Str. 31, D-97074 Würzburg, Germany
- ⁷³ Department of History of Science, Harvard University, Cambridge, MA 02138, USA
- ⁷⁴ Department of Physics, Harvard University, Cambridge, MA 02138, USA
- ⁷⁵ NCSA, University of Illinois, 1205 West Clark Street, Urbana, IL 61801, USA
- ⁷⁶ CP3-Origins, University of Southern Denmark, Campusvej 55, DK-5230 Odense M, Denmark
- ⁷⁷ Instituto Nacional de Astrofísica, Óptica y Electrónica. Apartado Postal 51 y 216, 72000. Puebla Pue., Mexico
- ⁷⁸ Consejo Nacional de Humanidades, Ciencia y Tecnología, Av. Insurgentes Sur 1582, 03940, Ciudad de México, Mexico
- ⁷⁹ Key Laboratory for Research in Galaxies and Cosmology, Chinese Academy of Sciences, Shanghai 200030, People's Republic of China
- ⁸⁰ Mizusawa VLBI Observatory, National Astronomical Observatory of Japan, 2-12 Hoshigaoka, Mizusawa, Oshu, Iwate 023-0861, Japan
- ⁸¹ Department of Astronomical Science, The Graduate University for Advanced Studies (SOKENDAI), 2-21-1 Osawa, Mitaka, Tokyo 181-8588, Japan
- ⁸² NOVA Sub-mm Instrumentation Group, Kapteyn Astronomical Institute, University of Groningen, Landleven 12, 9747 AD Groningen, The Netherlands
- ⁸³ Department of Astronomy, School of Physics, Peking University, Beijing 100871, People's Republic of China
- ⁸⁴ Kavli Institute for Astronomy and Astrophysics, Peking University, Beijing 100871, People's Republic of China
- ⁸⁵ Department of Astronomy, Graduate School of Science, The University of Tokyo, 7-3-1 Hongo, Bunkyo-ku, Tokyo 113-0033, Japan
- ⁸⁶ The Institute of Statistical Mathematics, 10-3 Midori-cho, Tachikawa, Tokyo, 190-8562, Japan
- ⁸⁷ Department of Statistical Science, The Graduate University for Advanced Studies (SOKENDAI), 10-3 Midori-cho, Tachikawa, Tokyo 190-8562, Japan
- ⁸⁸ Kavli Institute for the Physics and Mathematics of the Universe, The University of Tokyo, 5-1-5 Kashiwanoha, Kashiwa, 277-8583, Japan
- ⁸⁹ Leiden Observatory, Leiden University, Postbus 2300, 9513 RA Leiden, The Netherlands
- ⁹⁰ ASTRAVEO LLC, PO Box 1668, Gloucester, MA 01931, USA
- ⁹¹ Applied Materials Inc., 35 Dory Road, Gloucester, MA 01930, USA
- ⁹² Institute for Astrophysical Research, Boston University, 725 Commonwealth Avenue, Boston, MA 02215, USA
- ⁹³ University of Science and Technology, Gajeong-ro 217, Yuseong-gu, Daejeon 34113, Republic of Korea
- ⁹⁴ Institute for Cosmic Ray Research, The University of Tokyo, 5-1-5 Kashiwanoha, Kashiwa, Chiba 277-8582, Japan
- ⁹⁵ Joint Institute for VLBI ERIC (JIVE), Oude Hoogeveensedijk 4, 7991 PD Dwingeloo, The Netherlands
- ⁹⁶ Department of Astronomy and Atmospheric Sciences, Kyungpook National University, Daegu 702-701, Republic of Korea
- ⁹⁷ Department of Physics, Korea Advanced Institute of Science and Technology (KAIST), 291 Daehak-ro, Yuseong-gu, Daejeon 34141, Republic of Korea
- ⁹⁸ Kogakuin University of Technology & Engineering, Academic Support Center, 2665-1 Nakano, Hachioji, Tokyo 192-0015, Japan
- ⁹⁹ Graduate School of Science and Technology, Niigata University, 8050 Ikarashi 2-no-cho, Nishi-ku, Niigata 950-2181, Japan
- ¹⁰⁰ Physics Department, National Sun Yat-Sen University, No. 70, Lien-Hai Road, Kaosiung City 80424, Taiwan, R.O.C.
- ¹⁰¹ School of Astronomy and Space Science, Nanjing University, Nanjing 210023, People's Republic of China
- ¹⁰² Key Laboratory of Modern Astronomy and Astrophysics, Nanjing University, Nanjing 210023, People's Republic of China
- ¹⁰³ INAF-Istituto di Radioastronomia, Via P. Gobetti 101, I-40129 Bologna, Italy
- ¹⁰⁴ INAF-Istituto di Radioastronomia & Italian ALMA Regional Centre, Via P. Gobetti 101, I-40129 Bologna, Italy
- ¹⁰⁵ Instituto de Radioastronomía y Astrofísica, Universidad Nacional Autónoma de México, Morelia 58089, Mexico
- ¹⁰⁶ Yunnan Observatories, Chinese Academy of Sciences, 650011 Kunming, Yunnan Province, People's Republic of China
- ¹⁰⁷ Center for Astronomical Mega-Science, Chinese Academy of Sciences, 20A Datun Road, Chaoyang District, Beijing, 100012, People's Republic of China
- ¹⁰⁸ Key Laboratory for the Structure and Evolution of Celestial Objects, Chinese Academy of Sciences, 650011 Kunming, People's Republic of China
- ¹⁰⁹ Anton Pannekoek Institute for Astronomy, University of Amsterdam, Science Park 904, 1098 XH, Amsterdam, The Netherlands
- ¹¹⁰ Gravitation and Astroparticle Physics Amsterdam (GRAPPA) Institute, University of Amsterdam, Science Park 904, 1098 XH Amsterdam, The Netherlands
- ¹¹¹ Department of Astrophysical Sciences, Peyton Hall, Princeton University, Princeton, NJ 08544, USA
- ¹¹² School of Physics and Astronomy, Shanghai Jiao Tong University, 800 Dongchuan Road, Shanghai, 200240, People's Republic of China
- ¹¹³ National Institute of Technology, Hachinohe College, 16-1 Uwanotai, Tamonoki, Hachinohe City, Aomori 039-1192, Japan
- ¹¹⁴ Research Center for Astronomy, Academy of Athens, Soranou Efessiou 4, 115 27 Athens, Greece
- ¹¹⁵ Department of Physics, Villanova University, 800 Lancaster Avenue, Villanova, PA 19085, USA
- ¹¹⁶ Physics Department, Washington University, CB 1105, St. Louis, MO 63130, USA
- ¹¹⁷ Departamento de Matemática da Universidade de Aveiro and Centre for Research and Development in Mathematics and Applications (CIDMA), Campus de Santiago, 3810-193 Aveiro, Portugal
- ¹¹⁸ School of Physics, Georgia Institute of Technology, 837 State Street NW, Atlanta, GA 30332, USA
- ¹¹⁹ School of Space Research, Kyung Hee University, 1732, Deogyong-daero, Giheung-gu, Yongin-si, Gyeonggi-do 17104, Republic of Korea
- ¹²⁰ Canadian Institute for Theoretical Astrophysics, University of Toronto, 60 St. George Street, Toronto, ON M5S 3H8, Canada
- ¹²¹ Dunlap Institute for Astronomy and Astrophysics, University of Toronto, 50 St. George Street, Toronto, ON M5S 3H4, Canada
- ¹²² Canadian Institute for Advanced Research, 180 Dundas Street West, Toronto, ON M5G 1Z8, Canada
- ¹²³ Dipartimento di Fisica, Università di Trieste, I-34127 Trieste, Italy
- ¹²⁴ INFN Sez. di Trieste, I-34127 Trieste, Italy
- ¹²⁵ Department of Physics, National Taiwan Normal University, No. 88, Sec. 4, Tingzhou Road, Taipei 116, Taiwan, R.O.C.
- ¹²⁶ Center of Astronomy and Gravitation, National Taiwan Normal University, No. 88, Sec. 4, Tingzhou Road, Taipei 116, Taiwan, R.O.C.
- ¹²⁷ Gemini Observatory/NSF's NOIRLab, 670 North A'ohoku Place, Hilo, HI 96720, USA
- ¹²⁸ Department of Physics, University of Toronto, 60 St. George Street, Toronto, ON M5S 1A7, Canada
- ¹²⁹ Department of Physics, Tokyo Institute of Technology, 2-12-1 Ookayama, Meguro-ku, Tokyo 152-8551, Japan
- ¹³⁰ Hiroshima Astrophysical Science Center, Hiroshima University, 1-3-1 Kagamiyama, Higashi-Hiroshima, Hiroshima 739-8526, Japan
- ¹³¹ Aalto University Department of Electronics and Nanoengineering, PL 15500, FI-00076 Aalto, Finland
- ¹³² Jeremiah Horrocks Institute, University of Central Lancashire, Preston PR1 2HE, UK
- ¹³³ National Biomedical Imaging Center, Peking University, Beijing 100871, People's Republic of China
- ¹³⁴ College of Future Technology, Peking University, Beijing 100871, People's Republic of China
- ¹³⁵ Tokyo Electron Technology Solutions Limited, 52 Matsunagane, Iwayado, Esashi, Oshu, Iwate 023-1101, Japan
- ¹³⁶ Department of Physics and Astronomy, University of Lethbridge, Lethbridge, AB T1K 3M4, Canada
- ¹³⁷ Frontier Research Institute for Interdisciplinary Sciences, Tohoku University, Sendai 980-8578, Japan
- ¹³⁸ Astronomical Institute, Tohoku University, Sendai 980-8578, Japan
- ¹³⁹ Department of Physics and Astronomy, Seoul National University, Gwanak-gu, Seoul 08826, Republic of Korea
- ¹⁴⁰ University of New Mexico, Department of Physics and Astronomy, Albuquerque, NM 87131, USA
- ¹⁴¹ Physics Department, Brandeis University, 415 South Street, Waltham, MA 02453, USA
- ¹⁴² Tuorla Observatory, Department of Physics and Astronomy, University of Turku, Finland
- ¹⁴³ Radboud Excellence Fellow of Radboud University, Nijmegen, The Netherlands

¹⁴⁴ School of Natural Sciences, Institute for Advanced Study, 1 Einstein Drive, Princeton, NJ 08540, USA

¹⁴⁵ School of Physics, Huazhong University of Science and Technology, Wuhan, Hubei, 430074, People's Republic of China

¹⁴⁶ Mullard Space Science Laboratory, University College London, Holmbury St. Mary, Dorking, Surrey, RH5 6NT, UK

¹⁴⁷ Center for Astronomy and Astrophysics and Department of Physics, Fudan University, Shanghai 200438, People's Republic of China

¹⁴⁸ Astronomy Department, University of Science and Technology of China, Hefei 230026, People's Republic of China

¹⁴⁹ Department of Physics and Astronomy, Michigan State University, 567 Wilson Road, East Lansing, MI 48824, USA

Received 2024 April 30; revised 2024 June 23; accepted 2024 June 24; published 2024 August 27

Abstract

The first very long baseline interferometry (VLBI) detections at $870\ \mu\text{m}$ wavelength (345 GHz frequency) are reported, achieving the highest diffraction-limited angular resolution yet obtained from the surface of the Earth and the highest-frequency example of the VLBI technique to date. These include strong detections for multiple sources observed on intercontinental baselines between telescopes in Chile, Hawaii, and Spain, obtained during observations in 2018 October. The longest-baseline detections approach $11\ \text{G}\lambda$, corresponding to an angular resolution, or fringe spacing, of $19\ \mu\text{as}$. The Allan deviation of the visibility phase at $870\ \mu\text{m}$ is comparable to that at $1.3\ \text{mm}$ on the relevant integration timescales between 2 and 100 s. The detections confirm that the sensitivity and signal chain stability of stations in the Event Horizon Telescope (EHT) array are suitable for VLBI observations at $870\ \mu\text{m}$. Operation at this short wavelength, combined with anticipated enhancements of the EHT, will lead to a unique high angular resolution instrument for black hole studies, capable of resolving the event horizons of supermassive black holes in both space and time.

Unified Astronomy Thesaurus concepts: [Very long baseline interferometry \(1769\)](#); [Radio interferometry \(1346\)](#); [Black holes \(162\)](#); [Supermassive black holes \(1663\)](#); [High angular resolution \(2167\)](#); [Astronomical techniques \(1684\)](#); [Event horizons \(479\)](#)

1. Introduction

The technique of very long baseline interferometry (VLBI) involves a network of independently clocked telescopes separated by large distances, which simultaneously observe a common astronomical source (Thompson et al. 2017). The angular resolution, or fringe spacing, in a VLBI observation scales inversely with both the distance between stations (i.e., the length of the baseline) and the observing frequency. The present article reports the first fringe detections made at $870\ \mu\text{m}$ wavelength (345 GHz nominal frequency), which constitutes the shortest-wavelength VLBI observation to date. The experiment we describe was intended as a first technical demonstration of the $870\ \mu\text{m}$ VLBI capability using facilities that are part of the Event Horizon Telescope (EHT) array. Figure 1 shows the stations that participated in the fringe test along with the usual metric used to characterize millimeter-wavelength observing conditions: the 225 GHz zenith opacity (Thompson et al. 2017).

The VLBI observing wavelength has decreased over time. The first 3 mm VLBI detections (at 86 GHz) were obtained through observations performed in 1981 (Readhead et al. 1983), the first 3 mm intercontinental detections (100 GHz) were obtained through observations performed in 1988 (Baath et al. 1991, 1992), and the first successful 1.3 mm (230 GHz) VLBI was carried out in 1989 (Padin et al. 1990). The especially long time since the last significant decrease in VLBI wavelength reflects the challenges of carrying out such observations, which are detailed below. Even so, there have been several milestones of note since the early 1990s on the path toward developing short-wavelength VLBI as an

important technique for astrophysics. Increased sensitivity through the use of larger telescopes and advanced receivers led to 1.4 mm (215 GHz) detections on a $\sim 1100\ \text{km}$ baseline of multiple active galactic nuclei (AGN) and Sagittarius A* (Sgr A*), the Galactic center supermassive black hole (Greve et al. 1995; Krichbaum et al. 1997, 1998). A return to the longer-wavelength 2 mm spectral windows (147 GHz and 129 GHz) allowed extension of millimeter-wavelength VLBI to intercontinental baselines (Doeleman et al. 2002; Greve et al. 2002; Krichbaum et al. 2002). Building on this work, Doeleman et al. (2008, 2012) used purpose-built wideband digital VLBI systems on 1.3 mm transoceanic baselines to report the discovery of event-horizon-scale structures in Sgr A* and the much more massive black hole, M87*. The EHT collaboration has now imaged both of these sources with a global 1.3 mm VLBI array (Event Horizon Telescope Collaboration et al. 2019a, 2022a, 2024).

The EHT is the highest-resolution ground-based VLBI instrument to date (Event Horizon Telescope Collaboration et al. 2019b). The EHT fringe spacing is approximately $25\ \mu\text{as}$ at 1.3 mm wavelength. The finite diameter of the Earth limits ground-based 1.3 mm fringe spacing to $21\ \mu\text{as}$, corresponding to a $9.8\ \text{G}\lambda$ baseline. In practice, modern imaging methods, such as regularized maximum likelihood, achieve a slightly higher angular resolution that exceeds the diffraction limit (Event Horizon Telescope Collaboration et al. 2019c).

For future campaigns, the EHT has developed the capability to observe at $870\ \mu\text{m}$, and enhancing the ability to observe at this wavelength through new stations and wider bandwidth is an important aspect of long-term enhancements envisaged by the next-generation EHT (ngEHT) project (Doeleman et al. 2019, 2023; Raymond et al. 2021). For a given set of station locations, observing at $870\ \mu\text{m}$ improves angular resolution by approximately 50% compared to observing at 1.3 mm, which will provide a sharper view of the black hole shadow and environment; the $870\ \mu\text{m}$ fringe spacing limit set by the diameter of the Earth is approximately $14\ \mu\text{as}$, corresponding to a $14.7\ \text{G}\lambda$ baseline. Observations at $870\ \mu\text{m}$ are also important

¹⁵⁰ NASA Hubble Fellowship Program, Einstein Fellow.

¹⁵¹ Corresponding author.



Original content from this work may be used under the terms of the [Creative Commons Attribution 4.0 licence](#). Any further distribution of this work must maintain attribution to the author(s) and the title of the work, journal citation and DOI.

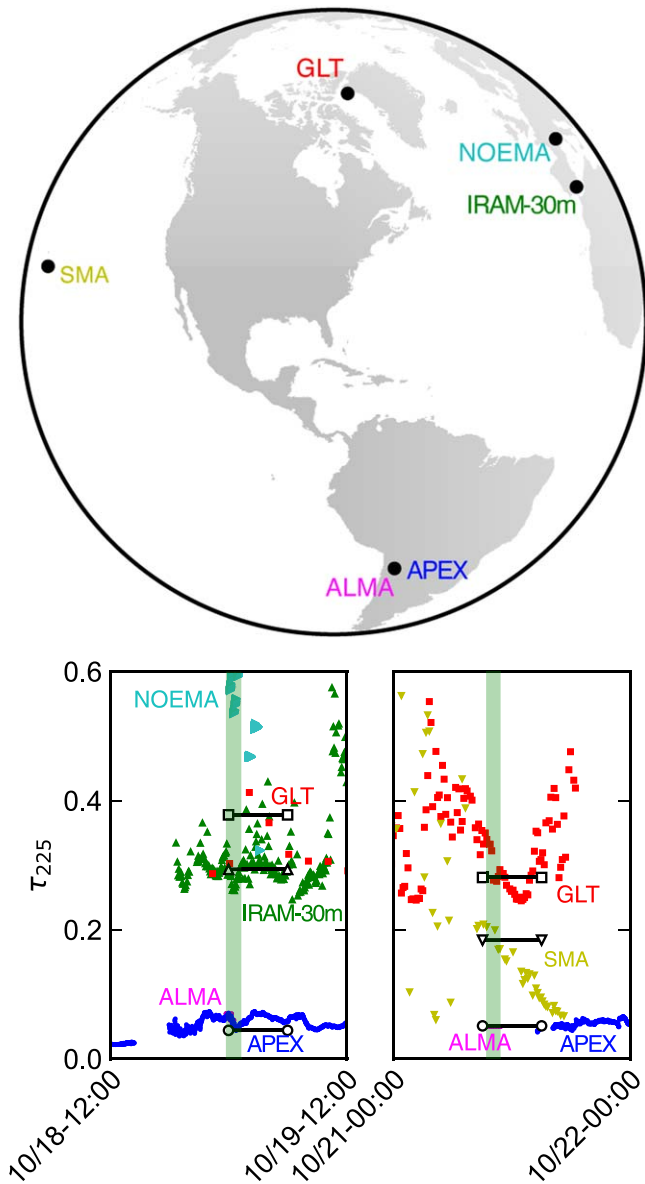


Figure 1. (Top) Stations in the $870\ \mu\text{m}$ fringe test. (Bottom) Zenith opacity at 225 GHz, which is the standard frequency used for monitoring millimeter-wave conditions. The observing window on each day is indicated by the green shading. Conditions at ALMA were very good during both days ($\tau_{225} \approx 0.05$). The black lines indicate the opacity at each site calculated using inputs from MERRA-2 reanalysis during the observing windows, which we use to estimate $870\ \mu\text{m}$ (345 GHz) opacity. Opacities for APEX and NOEMA have been estimated by converting precipitable water vapor column amounts.

for polarimetric measurements. Faraday rotation, which scrambles the imaged electric field vector position angle pattern, diminishes with the square of the frequency. Therefore, $870\ \mu\text{m}$ observations may help distinguish Faraday rotation from the intrinsic field pattern set by the horizon-scale magnetic field and plasma properties (Event Horizon Telescope Collaboration et al. 2021; Wielgus et al. 2024). For Sgr A*, the angular size of the black hole shadow is larger than that of M87* (Event Horizon Telescope Collaboration et al. 2022a), but scattering in the ionized interstellar medium affects the image angular resolution (see, e.g., Johnson et al. 2018). At 1.3 mm, the scatter broadening is comparable to the current EHT resolution, but it decreases approximately as the observing wavelength squared. Thus, at $870\ \mu\text{m}$, scattering

effects would be significantly diminished and would not limit the resolution of a VLBI array for studies of Sgr A*. In particular, extension of the EHT to $870\ \mu\text{m}$ wavelengths can target photon ring substructure in Sgr A*, aiming to detect the orbit of light that makes a full “u-turn” around the black hole (Johnson et al. 2020; Palumbo et al. 2023). For these reasons, $870\ \mu\text{m}$ VLBI opens important new directions for advanced horizon-resolved studies of the two primary EHT sources. At the same time, higher-frequency VLBI brings more sources into range for horizon-resolved black hole studies (Pesce et al. 2021; Lo et al. 2023; Ramakrishnan et al. 2023), and the increased resolution at $870\ \mu\text{m}$ benefits nonhorizon VLBI studies of AGN jets (e.g., Kim et al. 2020; Janssen et al. 2021; Issaoun et al. 2022; Jorstad et al. 2023; Paraschos et al. 2024). Additionally, due to reduced opacity, shorter wavelengths probe more compact regions of jetted AGN sources (an example being the core-shift effect; Lobanov 1998; Hada et al. 2011). Hence, $870\ \mu\text{m}$ VLBI has the potential to image the jet launching region closer to the central black hole, enabling investigations of the physics behind jet formation, collimation, and acceleration. In particular, the poorly understood limb brightening in transversely resolved inner jets (e.g., Janssen et al. 2021) can be studied in much greater detail.

Extension of observing to $870\ \mu\text{m}$ similarly enhances the capability of the EHT to capture dynamics near the event horizon. In the case of Sgr A*, the dynamical timescale is $\sim 200\ \text{s}$ ($10GM/c^3$). Simultaneous 1.3 mm and $870\ \mu\text{m}$ observing can sample sufficient Fourier spatial frequencies within this integration time to allow snapshot imaging using the technique of multifrequency synthesis (MFS; Chael et al. 2023). Combining such snapshots will enable recovery of accretion and jet launching kinematics. For M87*, the dynamical timescale is ~ 3 days, and data obtained in both 1.3 mm and $870\ \mu\text{m}$ on sequential days can be combined to form high-fidelity MFS images for time-lapse movie reconstruction of the event horizon environment. Realizing the full scientific potential of $870\ \mu\text{m}$ VLBI (Johnson et al. 2023) will require the planned ngEHT upgrade (Doeleman et al. 2023).

While there are clearly many motivating reasons for $870\ \mu\text{m}$ VLBI observing, a number of factors make the measurements difficult in this short-wavelength regime. The atmosphere is more opaque at $870\ \mu\text{m}$ than at 1.3 mm (see, for example, Liebe 1985; Matsushita et al. 1999, 2016, 2022), which means that sources are more attenuated and noise levels due to atmospheric emission are elevated. Overall, the effective system temperatures of coherent radio receivers are intrinsically greater at $870\ \mu\text{m}$ than at 1.3 mm.¹⁵² The aperture efficiency of the collecting optics tends to diminish at high frequency, and the source flux density tends to decrease. In addition, coherence losses due to the VLBI frequency standards used at each site increase with observing frequency (Doeleman et al. 2011). The EHT array, conceived as a common, international effort of independent observatories working in the short-millimeter range, has directly addressed these challenges and provides key enabling infrastructure for extension of VLBI to higher frequencies (Event Horizon Telescope Collaboration et al. 2019b).

The telescopes comprising the EHT array are precision structures sited at high-altitude, low-opacity locations (see, e.g., Levy et al. 1996; Mangum et al. 2006; Greve & Bremer 2010; Chen et al. 2023 and references therein on the design and

¹⁵² See, for example, Janssen et al. (2019) or the ALMA Cycle 8 2021 Technical Handbook.

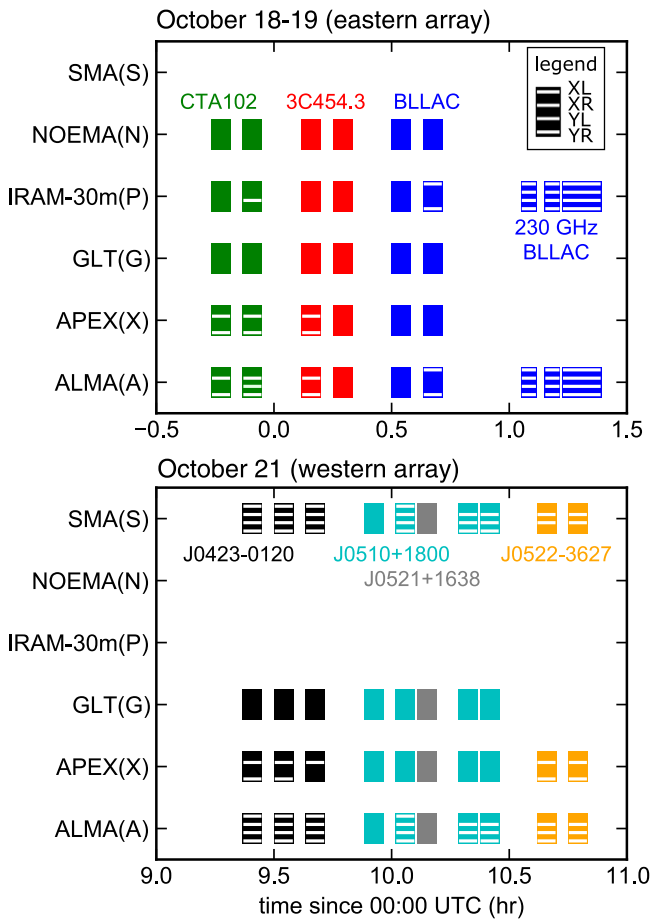


Figure 2. 870 μm observations that yielded detections were made during two separate scheduling blocks: 2018 October 18/19 and 2018 October 21. The observations on the first night were done with an eastern array comprising ALMA, APEX, GLT, IRAM30m, and NOEMA. Observations on the second night were made with a western array: ALMA, APEX, GLT, and SMA. The scheduling blocks for both nights are shown along with the one-letter station codes, which are listed in parentheses. All detections are on baselines involving ALMA. The scans that yielded detections on baselines defined by a given station are indicated by the white horizontal ticks centered in each time block: from the top, ticks correspond to XL, XR, YL, and YR mixed polarizations per the legend at upper right. The absence of a tick indicates a nondetection. Three scans at 230 GHz (1.3 mm) were performed at the end of the eastern subarray scheduling block using just the IRAM30m and ALMA facilities.

qualification of such instruments). State-of-the-art instrumentation underpinning the operation of these telescopes, as single-dish facilities and for VLBI, includes cryogenic receivers and wideband digital backends—all refined over many years to optimize performance at millimeter and submillimeter wavelengths. Steady improvements in superconductor–insulator–superconductor junctions have formed the basis for increased bandwidth and sensitivity of millimeter and submillimeter receivers, leading to state-of-the-art systems in use at EHT sites (see Maier et al. 2005, 2012; Tong et al. 2005, 2013; Chenu et al. 2007, 2016; Carter et al. 2012; Mahieu et al. 2012; Kerr et al. 2014; Klein et al. 2014; Belitsky et al. 2018; Han et al. 2018).

Following the successful 1.3 mm VLBI observations in 2017, test observations at 870 μm were conducted on the EHT array in 2018 October. Conditions at the Atacama Large Millimeter/submillimeter Array (ALMA) station during this test, including characterization of the system used there to

phase the array for VLBI, are described in Crew et al. (2023). The present paper describes the VLBI test observations

2. Methods

2.1. Schedule

The 870 μm fringe test observations consisted of two short scheduling blocks designed for two different subarrays. An eastern subarray, comprising ALMA, the Atacama Pathfinder EXperiment (APEX), the Greenland Telescope (GLT), the Institut de Radioastronomie Millimétrique 30 m telescope (IRAM30m), and the Northern Extended Millimeter Array (NOEMA), was scheduled to include blazar sources that were visible in the nighttime hours at all sites: CTA 102, 3C 454.3, and BL Lac. A western subarray, comprising ALMA, APEX, GLT, and the Submillimeter Array (SMA), observed quasars J0423–0120, J0510+1800, J0521+1638, and J0522–3627. The eastern subarray scheduling block was followed by several scans on BL Lac at 1.3 mm wavelength to aid diagnosis in the event of a null result. Schedule blocks for both subarrays were optimized for fringe detection at 870 μm VLBI, and they spanned a duration of between 1 and 2 hr with at least two scans on every source. Most scans lasted 5 minutes.

The observing window consisted of five nights, 2018 October 17–21, between approximately midnight and 2:00 Coordinated Universal Time (UTC) for the eastern subarray scheduling block and between 9:00 and 11:00 UTC for the western subarray scheduling block. Each scheduling block was triggered twice within the observing window. We report herein on successful observations with the eastern array on 2018 October 18–19 and with the western array on 2018 October 21. Details of the scheduling blocks and sources observed are shown in Figure 2.

2.2. Instrumentation and Array

Several important technologies developed for 1.3 mm VLBI are leveraged to address the challenges of 870 μm observing, many of which are outlined in Event Horizon Telescope Collaboration et al. (2019b). The VLBI backends, used to condition and digitize signals from the telescope receivers, have a cumulative data rate of 64 Gbps (Vertatschitsch et al. 2015; Tuccari et al. 2017) across four 2 GHz wide bands and two polarizations. Each station is outfitted with a hydrogen maser time standard, which had previously been found to be sufficiently stable for timekeeping in a 1.3 mm VLBI experiment and was expected to be sufficiently stable for 870 μm .

Phased array beamforming capability is implemented at both the SMA (Young et al. 2016) and ALMA (Matthews et al. 2018) array stations. For both these stations, beamformer phasing efficiency at 870 μm , which directly scales the visibility amplitudes measured on baselines to the station, varied from just below 50% to as high as about 80%. These efficiencies are less than what is typical for 1.3 mm (Event Horizon Telescope Collaboration et al. 2019b). Section 3.4 has a discussion relevant to ALMA, SMA, and NOEMA¹⁵³ of phasing efficiency challenges and planned improvements to mitigate these.

¹⁵³ NOEMA is also equipped with the phased array, though it was not commissioned at the time of this observation.

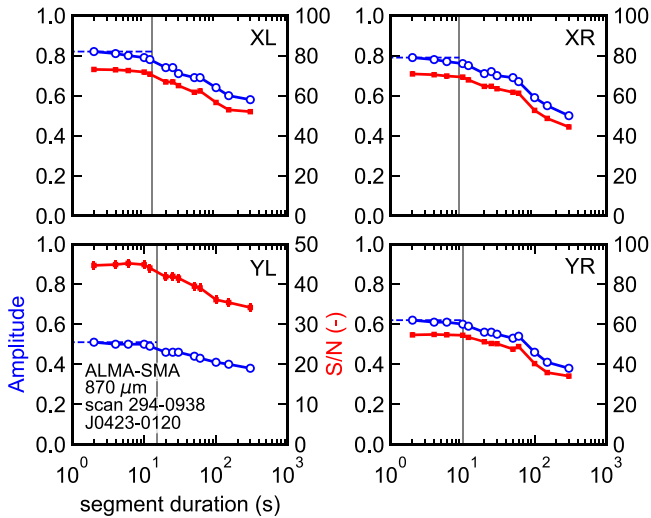


Figure 3. Scan-averaged and noise-debiased $870\ \mu\text{m}$ fringe amplitude (open blue circles, left axes) and S/N (filled red squares, right axes). Amplitudes and S/N are computed by first dividing each observing scan into short coherently integrated segments, which are then combined incoherently following the procedure in Rogers et al. (1995). Segment length is shown on the horizontal axis. Each subplot shows a different polarization on the ALMA–SMA baseline for a single scan on J0423–0120 (October 21, 09:38 UTC). Other detections listed in Table 1 have a similar dependence on segment duration but generally lower S/N. The noise-debiased amplitude and coherence time were derived using HOPS and are indicated by the horizontal blue dashed line and the vertical solid black line, respectively.

The frequency setup for the $870\ \mu\text{m}$ fringe test is similar to that described in Table 4 of Event Horizon Telescope Collaboration et al. (2019b). Most stations in the array observed a single 2048 MHz band at a 4–6 GHz intermediate frequency (IF) using a 342.6 GHz sky local oscillator (LO).¹⁵⁴ That frequency setup corresponds to a sky frequency range of 346.552–348.6 GHz. Each station observed both circular polarizations, with the exceptions of APEX (right-circular polarization only) and ALMA (dual linear, X and Y). The recorded station data were correlated using DiFX software (Deller et al. 2011) at the MIT Haystack Observatory. Visibility data on baselines to ALMA remained on a mixed-polarization basis (i.e., $\{X, Y\} \times \{L, R\}$) because the observing schedules were not long enough to track polarization calibrators over a wide range of parallactic angles, which is necessary for converting the ALMA data from a linear to a circular basis (Martí-Vidal et al. 2016; Matthews et al. 2018; Goddi et al. 2019). Subsequent fringe fitting was done using the Haystack Observatory Postprocessing System (HOPS¹⁵⁵; Whitney et al. 2004; see also Blackburn et al. 2019).

2.2.1. ALMA

ALMA observed in dual linear polarization with IRAM-designed $870\ \mu\text{m}$ (i.e., Band 7) cartridges (Mahieu et al. 2012). The ALMA Phasing System (APS; Matthews et al. 2018) was used to aggregate the collecting area of the active dishes in the ALMA array. The APS capability had been used previously for VLBI science at 3 mm (Issaoun et al. 2019; Okino et al. 2022; Zhao et al. 2022) and 1.3 mm (Event Horizon Telescope Collaboration et al. 2019a, 2019b) but not at shorter

¹⁵⁴ ALMA and SMA used slightly different frequency setups to match the sky frequency of the other stations; see Sections 2.2.1 and 2.2.6.

¹⁵⁵ <https://www.haystack.mit.edu/tech/vlbi/hops.html>

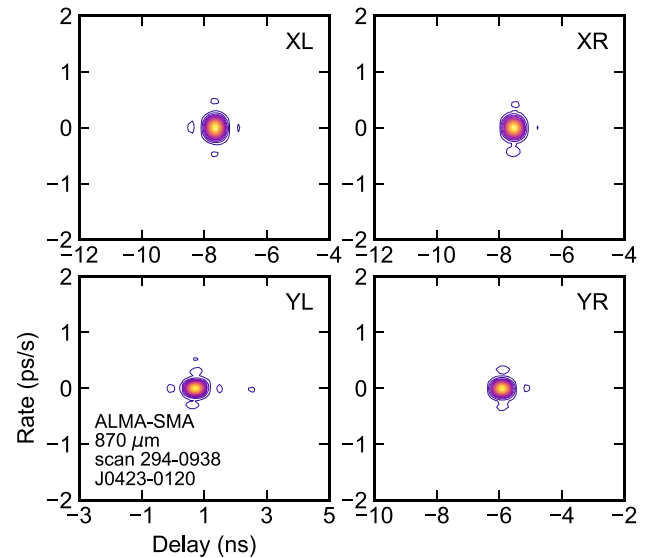


Figure 4. $870\ \mu\text{m}$ contours of incoherently averaged fringe power in 5% increments vs. delay and rate for a single scan on J0423–0120 for the ALMA–SMA baseline (October 21, 09:38 UTC). Other detections reported in Table 1 also exhibit clear peaks vs. delay/rate.

wavelengths, albeit the setup for $870\ \mu\text{m}$ observations is similar to the longer-wavelength bands. In the $870\ \mu\text{m}$ experiment, the four recorded 2.048 GHz subbands were tuned to center frequencies of 335.6, 337.541406, 347.6, and 349.6 GHz. The choice of the 337.541406 GHz frequency results from ALMA-specific tuning restrictions.

The ALMA phased array included 25 12 m antennas during the eastern track and 29 12 m antennas during the western track with a maximum antenna spacing of 600 m in both cases. Wind speeds were greater than $10\ \text{m s}^{-1}$ at the ALMA site. During the eastern track, the phasing efficiency was below 50% for most of the time and at best was about 80%. During the October 21 track (western) in better weather, the phasing efficiency was more stable and greater than approximately 90% (Crew et al. 2023).

2.2.2. APEX

The APEX and ALMA stations are colocated, and conditions were similar at the two telescopes. APEX observed using the 345 GHz FLASH+ linear receiver (Klein et al. 2014). That receiver may not have been functioning optimally during the experiment and has since been replaced by the Swedish-ESO PI Instrument for APEX (Belitsky et al. 2018; Meledin et al. 2022). A quarter wave plate was used to achieve circular polarization. Two backends, a ROACH2 Digital Backend (R2DBE; Vertatschitsch et al. 2015) and a Digital BaseBand Converter 3 (Tuccari et al. 2017), were operated in parallel.

2.2.3. GLT

The GLT station participated in the observation but at the time was still commissioning specific subsystems. The GLT antenna has operated at Pituffik Space Base, formerly the Thule Airbase site, in Greenland since 2017 August (Inoue et al. 2014; Raffin et al. 2016; Matsushita et al. 2018; Koay et al. 2020; Chen et al. 2023). The GLT observed in dual linear polarization with the IRAM-made $870\ \mu\text{m}$ (i.e., Band 7) cartridges (Mahieu et al. 2012). The 345 GHz receiver on the GLT saw first light in continuum and spectral-line modes in

Table 1
870 μm Detections on the Indicated Baselines, Sources, and Polarizations

Baseline ^a	Pol.	Day ^b	Time (hh:ss)	El. 1 (deg)	El. 2 (deg)	$ \bar{u} - \bar{v} $ (G λ)	τ_c (s)	Delay (ns)	Rate (fs s ⁻¹)	Amp. ($\times 10^{-4}$)	S/N
3C 454.3											
AX	XR	292	00:07	44.9	45.0	0.0026	8	4.4	-1	0.50	43.7
AX	YR	292	00:07	44.9	45.0	0.0026	8	5.2	-1	0.47	41.4
BL Lac											
AP	XL	292	00:38	24.6	42.6	9.7913	31	-4.6	4	0.15	12.2
AP	YR	292	00:38	24.6	42.6	9.7913	46	-8.5	0	0.13	10.8
CTA 102											
AP	YL	291	23:52	49.7	43.5	9.9581	21	0.9	-38	0.18	13.6
AX	XR	291	23:44	48.6	48.7	0.0027	24	5.6	-38	0.23	19.2
AX	XR	291	23:52	49.7	49.7	0.0027	10	5.2	-85	0.23	20.8
AX	YR	291	23:44	48.6	48.7	0.0027	22	6.3	-51	0.21	17.6
AX	YR	291	23:52	49.7	49.7	0.0027	11	6.0	-84	0.22	18.0
J0423-0120											
AS	XL	294	09:22	48.5	35.5	10.8547	14	-7.6	6	0.54	47.8
AS	XL	294	09:30	46.8	37.3	10.8874	14	-8.0	0	0.70	62.4
AS	XL	294	09:38	45.1	39.1	10.9100	13	-7.7	-2	0.82	73.1
AS	XR	294	09:22	48.5	35.5	10.8547	9	-7.5	19	0.60	53.4
AS	XR	294	09:30	46.8	37.3	10.8874	34	-7.9	-0	0.64	56.6
AS	XR	294	09:38	45.1	39.1	10.9100	9	-7.5	-2	0.79	70.8
AS	YL	294	09:22	48.5	35.5	10.8547	13	0.8	19	0.34	29.6
AS	YL	294	09:30	46.8	37.3	10.8874	17	0.4	0	0.47	41.3
AS	YL	294	09:38	45.1	39.1	10.9100	15	0.7	-2	0.51	45.2
AS	YR	294	09:22	48.5	35.5	10.8547	10	-5.9	19	0.46	40.7
AS	YR	294	09:30	46.8	37.3	10.8874	14	-6.3	0	0.50	44.2
AS	YR	294	09:38	45.1	39.1	10.9100	10	-5.9	-3	0.62	54.9
AX	XR	294	09:22	48.5	48.5	0.0028	27	-1.0	-8	0.14	12.6
AX	XR	294	09:30	46.8	46.8	0.0028	39	-0.9	-9	0.16	13.0
AX	XR	294	09:38	45.1	45.1	0.0028	32	-0.9	-11	0.15	12.9
AX	YR	294	09:22	48.5	48.5	0.0028	30	0.6	-7	0.14	10.9
AX	YR	294	09:30	46.8	46.8	0.0028	29	0.7	-9	0.14	10.8
J0510+1800											
AS	XL	294	10:01	37.0	39.6	10.9218	30	-8.0	-12	0.10	8.5
AS	XR	294	10:01	37.0	39.6	10.9218	28	-8.0	-12	0.25	22.3
AS	XR	294	10:17	34.5	43.4	10.8891	8	-8.1	-0	0.27	22.4
AS	XR	294	10:22	33.5	44.8	10.8682	22	2.2	20	0.20	16.6
AS	YL	294	10:01	37.0	39.6	10.9218	10	0.3	-12	0.20	18.1
AS	YL	294	10:17	34.5	43.4	10.8891	23	0.2	11	0.25	21.3
AS	YL	294	10:22	33.5	44.8	10.8682	29	-6.6	2	0.17	14.2
AS	YR	294	10:01	37.0	39.6	10.9218	28	-6.3	-14	0.12	10.1
AS	YR	294	10:17	34.5	43.4	10.8891	6 ^c	-6.5	0	0.14	11.5
AS	YR	294	10:22	33.5	44.8	10.8682	10 ^c	3.8	81	0.11	9.7
J0522-3627											
AS	XR	294	10:37	53.0	18.0	10.3188	12 ^c	-4.7	38	0.12	10.1
AS	XR	294	10:45	51.4	19.2	10.4084	24	-4.9	8	0.20	12.1
AS	YL	294	10:37	53.0	18.0	10.3188	29	3.5	-4	0.12	10.3
AS	YL	294	10:45	51.4	19.2	10.4084	22	3.4	-4	0.16	14.1
AX	XR	294	10:37	53.0	52.9	0.0030	31	0.8	-1	0.31	26.9
AX	XR	294	10:45	51.4	51.4	0.0030	39	0.8	25	0.25	15.3
AX	YR	294	10:37	53.0	52.9	0.0030	31	2.3	1	0.31	27.0
AX	YR	294	10:45	51.4	51.4	0.0030	31	2.4	25	0.29	24.6

Notes.^a Baselines: AX (ALMA-APEX), AP (ALMA-IRAM30m), AS (ALMA-SMA).^b Day of year in 2018.^c The S/N was insufficient to fit the coherence time. The reported value is the segmentation time that achieves the greatest S/N for the scan.

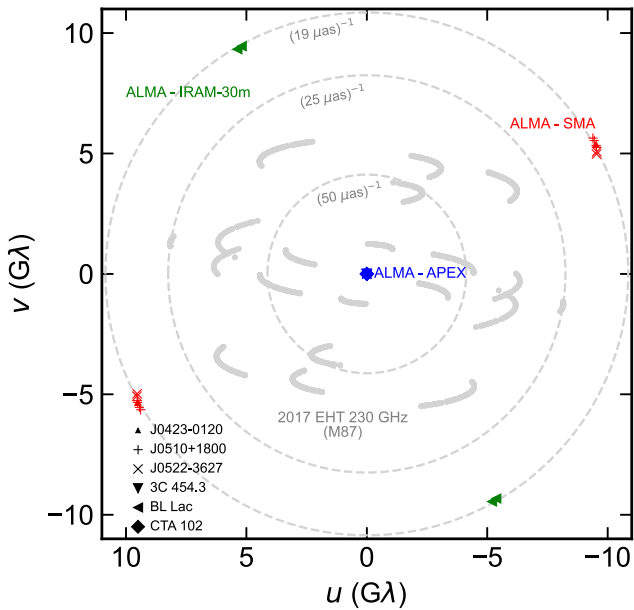


Figure 5. Detections on various targets at 345 GHz (see Table 1). The u - v locations of 230 GHz detections on M87* during the EHT 2017 April campaign are shown in gray including low-S/N scans at $(25 \mu\text{as})^{-1}$.

2018 August. Pointing and focus calibration at 345 GHz were still in the commissioning phase during the $870 \mu\text{m}$ observation reported here. The GLT pointing system has since been fully commissioned for recent and future VLBI observing. Similarly, final adjustments to the dish surface had yet to be made, and the surface accuracy was estimated to be $170 \mu\text{m}$ rms during the observations reported here. Subsequent improvements have led to rms surface accuracy in the 17 – $40 \mu\text{m}$ range (see Table 7 in Chen et al. 2023).

2.2.4. IRAM30m

The IRAM30m telescope used the heterodyne Eight Mixer Receiver (Carter et al. 2012) in the $870 \mu\text{m}$ band also known as E330. The setup and preobserving checks were analogous to a regular Global Millimeter VLBI Array or EHT session. The opacity at $870 \mu\text{m}$ during the scheduled VLBI observations was high and would not typically have triggered single-dish science operation at this wavelength.

2.2.5. NOEMA

Portions of the NOEMA station were still being commissioned during the $870 \mu\text{m}$ experiment. NOEMA observed in dual polarization as a single-antenna station, not as a phased array. The NOEMA receiver was a dual-polarization single-sideband unit (Chenu et al. 2016) with a 4 GHz bandpass. Recording was with a 16 Gbps R2DBE. The NOEMA phased array has since been commissioned for VLBI observing.

2.2.6. SMA

The SMA station observed with seven antennas arranged in the compact configuration with a maximum baseline of 69.1 m. The SMA Wideband Astronomical ROACH2 Machine (SWARM; Primiani et al. 2016; Young et al. 2016) was run with the VLBI beamformer mode activated, producing a coherent phased array sum of the seven antennas formatted for VLBI recording. As expected, the phasing efficiency was lower

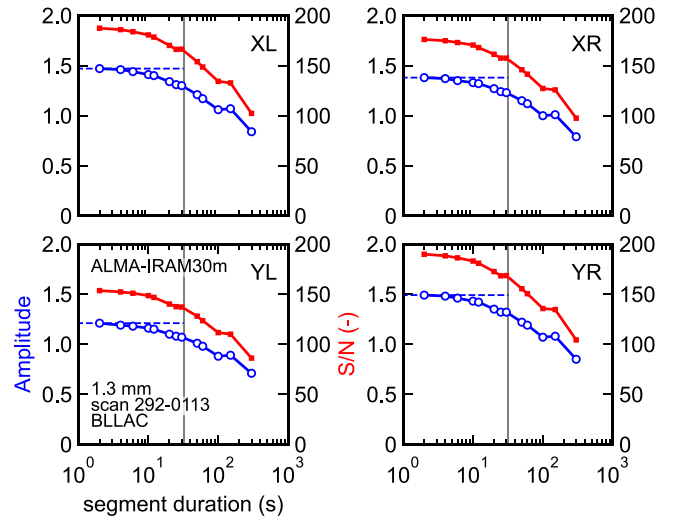


Figure 6. 1.3 mm amplitude (open blue circles, left axes) and S/N (filled red squares, right axes) vs. the duration of coherently integrated segments, which are incoherently averaged. Each subplot shows a different polarization on the baseline between ALMA and IRAM30m for a single scan on BL Lac on October 19, 01:13 UTC. Other BL Lac detections listed in Table 2 have a similar dependence on segment duration. The noise-debiased amplitude and coherence time were derived using HOPS and are indicated by the horizontal blue dashed line and the vertical solid black line, respectively. These data were calibrated in the same manner as the $870 \mu\text{m}$ detections.

than for 1.3 mm operations. The sky LO was set to 341.6 GHz, not 342.6 GHz, to match the SWARM sky coverage with the other stations, compensating for a different IF to baseband LO because SWARM uses its own block downconverter rather than the standard EHT single-dish equipment. The data were recorded in the frequency domain at the standard SMA clock rate (4.576 Gsps), which differs from the standard EHT single-dish sample rate of 4.096 Gsps (Vertatschitsch et al. 2015). Adaptive Phased Array Interpolating Downsampler for SWARM (APHIDS) postprocessing was completed to interpolate and invert (from frequency domain to time domain) the SWARM data sets in preparation for VLBI correlation. After APHIDS processing, the SMA EHT data product matches that produced by the standard SMA single-dish station in sample rate and is also a time series matching the standard EHT single-dish data product.

3. Results and Discussion

Figure 1 shows that the conditions during the experiment were mixed across the array. While the observatories do not measure $870 \mu\text{m}$ (345 GHz) opacity directly, we use MERRA-2 reanalysis and radiative transfer (Paine 2022) that is validated by measurements at 225 GHz (Figure 1, black lines) to estimate τ_{345} . For the eastern subarray on October 18/19, τ_{345} was 0.2 at the ALMA and APEX sites and 0.8 at IRAM30m. For the western subarray on October 21, τ_{345} was approximately 0.17 at the ALMA and APEX sites and 0.7 at SMA. During the experiment, the opacities at GLT and NOEMA were unfavorable, and detections on baselines to those stations were not achieved; however, both stations have weather that is compatible with $870 \mu\text{m}$ observing and will likely yield high-frequency detections in the future (see, e.g., Raymond et al. 2021; Matsushita et al. 2022). Atmospheric conditions can change rapidly: τ_{225} at the SMA decreased by nearly a factor of 4 in the hours following the experiment.

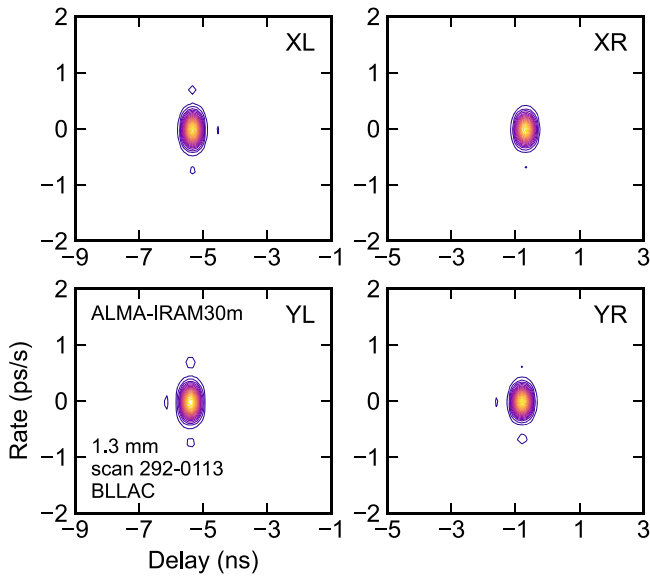


Figure 7. 1.3 mm contours of incoherently averaged fringe power in 5% increments vs. delay and rate for the baseline between ALMA and IRAM30m. This example is for a single scan on BL Lac taken on October 19, 01:13 UTC. Other detections reported in Table 2 also exhibit clear peaks vs. in delay-delay rate search space.

3.1. $870\ \mu\text{m}$ (345 GHz) Fringes

In VLBI, recorded data from all sites are brought to a central processing facility where data streams from each pair of sites are cross-correlated. The resulting complex correlation quantities provide a dimensionless measure of the electric field coherence between the two sites, which is proportional to a Fourier component of the brightness distribution of the target source. The correlation processor uses an a priori model to align the site data streams, recreating the exact geometry of the physical baseline connecting the two sites at the time of observation. Because the a priori model is imperfect, after processing, the cross-correlation phase typically varies as a function of time and frequency due to residual delay and delay rate, respectively. To average the correlation signal over frequency and time, the correlator output is thus searched over a range of delay and delay rate to find a peak in correlator power—a process also known as “fringe fitting” (Thompson et al. 2017). In this experiment, the correlator output was searched by dividing each scan into short segments and incoherently averaging them. The incoherent averaging technique (Rogers et al. 1995) estimates noise-debiased VLBI quantities, and it is well suited to processing low signal-to-noise ratio (S/N) VLBI data on sparse arrays as it allows integration beyond the nominal atmospheric coherence time. Figure 3 shows the dependence of amplitude in units of 10^4 and S/N on the duration of the segments for a sample scan on source J0423–0120 for the baseline comprising the ALMA and SMA stations. All four cross-hand polarizations are plotted. The scan identifier 294–0938 in Figure 3 corresponds to the day UTC for the beginning of the scan, where the day is the number of days since 2018 January 1 (294 is October 21) and UTC is the scan start time. The noise-debiased amplitude (Rogers et al. 1995) in Figure 3 is indicated by the horizontal blue dashed line. As the segment duration decreases, the effect of decoherence is reduced, so the S/N increases.

Compared to a single coherent integration over a full scan (approximately 300 s in most of the measurements),

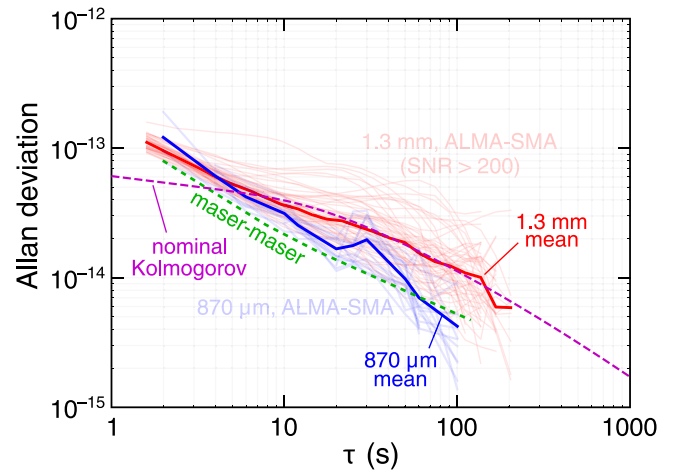


Figure 8. Allan deviation for $870\ \mu\text{m}$ (345 GHz) scans observed on the ALMA–SMA baseline (blue lines). For comparison, red lines show the Allan deviation for high-S/N scans (nominally 5 minutes long) during the 1.3 mm (230 GHz) 2017 EHT campaign (Event Horizon Telescope Collaboration et al. 2019b). Weather variability during the 2017 campaign is responsible for the spread in those scans. The means of the individual Allan deviation traces are shown in bold for the two frequencies. The $870\ \mu\text{m}$ and 1.3 mm mean traces approach the nominal Allan deviation for a pair of T4 Science brand iMaser 3000 model masers (Thompson et al. 2017) at short timescales. At intermediate timescales, atmospheric turbulence can become important. The Allan deviation associated with Kolmogorov turbulence is plotted for a set of nominal parameters (Treuhaft & Lanyi 1987).

Table 2
1.3 mm Detections on the ALMA–IRAM30m Baseline toward BL Lac for Indicated Polarizations

Elevation (ALMA/ IRAM30m) (deg)	Baseline Length (G λ)	τ_c (s)	Delay (ns)	Rate (fs s $^{-1}$)	Amp. ($\times 10^{-4}$)	S/N
XL						
24.5/38.3	6.4327	5	−5.3	−98	1.66	134.0
24.4/37.3	6.4422	7	−5.3	−66	1.49	120.0
24.3/36.6	6.4476	32	−5.3	−14	1.47	187.3
YR						
24.5/38.3	6.4327	6	−0.8	−99	1.77	143.0
24.4/37.3	6.4422	7	−0.8	−66	1.52	122.4
24.3/36.6	6.4476	32	−0.8	−14	1.49	189.8
XR						
24.5/38.3	6.4327	6	−0.7	−98	1.56	125.4
24.4/37.3	6.4422	7	−0.7	−66	1.37	110.4
24.3/36.6	6.4476	32	−0.7	−13	1.38	176.1
YL						
24.5/38.3	6.4327	6	−5.4	−98	1.42	114.4
24.4/37.3	6.4422	7	−5.4	−66	1.24	100.1
24.3/36.6	6.4476	32	−5.4	−14	1.21	153.5

Note. Scans listed top to bottom on October 19 begin at 01:03, 01:09, and 01:13 UTC.

incoherently averaging the parts of a segmented scan increases the S/N by up to a factor of 2 on many of the measurements, yielding higher confidence in the detections. For most of the measurements, S/N values asymptote at the shortest segment

durations. Ordinarily, we would expect the S/N values to decrease as the segments are shortened below the coherence time. The behavior we observe could be indicative of a changing coherence during the scan consistent with the windy conditions at ALMA (Crew et al. 2023).

Contours of fringe power versus multiband delay and rate are plotted in Figure 4 for a single scan of J0423–0120 on the ALMA–SMA baseline. The measurement exhibits a definitive peak in fringe power for each of the cross-hand polarizations. The rates are all centered near 0. Multiband delays fall within an ambiguity search window of (–8.53 ns, 8.53 ns) as they are derived from measurements spaced at ALMA’s channel separation of 58.592375 MHz (Matthews et al. 2018; Event Horizon Telescope Collaboration et al. 2019d).

The fringe detection threshold was conservatively set at $S/N > 7$ to prevent false detections, and all resulting detections are summarized in Table 1 ordered by target source. The maximum spatial frequencies sampled are greater than $10.9 \text{ G}\lambda$ between ALMA and the SMA, which significantly exceeds the largest spatial frequencies sampled by the EHT for M87* at 1.3 mm on the longest baseline between Hawaii and Europe (approximately $8 \text{ G}\lambda$). The highest-S/N detections exceed 70. Simultaneous detections in all four polarization products were achieved on the ALMA–SMA baseline for J0423–0120. The zero-baseline flux densities at $870 \mu\text{m}$ were obtained from the ALMA local interferometry (Crew et al. 2023). The flux densities were 1.4, 1.0, 2.4, 1.2, and 4.9 Jy on CTA 102, BL Lac, J0423–0120, J0510+1800, and J0522–3627, respectively. The source structure of the targets in this work is not known a priori, so it is not possible to say with precision how the correlated amplitudes should vary as a function of baseline length. Furthermore, these observations were designed to be a detection experiment and not carried out with all procedures that would allow robust VLBI flux density calibration. Nevertheless, the S/N on the ALMA–APEX baselines appears to be anomalously low given the short baseline length, which would ordinarily be sensitive to both small-scale structure (10–100 μas) and larger-scale structure (10–100 mas). This is likely attributable to phase instabilities suspected in the APEX receiver (see Section 2.2.2), which has since been retired. Follow-on experiments, already scheduled, will focus on calibration and robust flux density measurements versus baseline length.

HOPS reports two coherence times: one corresponding to the point below which there is only a small amount of coherence loss within the uncertainty of amplitudes and another corresponding to the maximum S/N. For most of the scans in Table 1, we report the former. In a few low-S/N cases where the routine was unable to fit the coherence, the coherence time based on S/N is reported instead. The coherence times across baselines range from approximately 10 to 30 s for most cases. For BL Lac, the longer coherence times may be an artifact of the moderate S/N.

3.2. 1.3 mm (230 GHz) Comparison

Presently, the EHT observes at 1.3 mm (Event Horizon Telescope Collaboration et al. 2019b). Figure 5 compares the Fourier components of the $870 \mu\text{m}$ detections on various sources to the 1.3 mm coverage of the 2017 EHT array on M87* (Event Horizon Telescope Collaboration et al. 2019d). The $870 \mu\text{m}$ detections on ALMA–IRAM30m and ALMA–SMA baselines have a higher nominal angular resolution

(19 μas) than the highest-resolution M87* detections (nominally 25 μas).

For a source-specific comparison of the 1.3 mm and $870 \mu\text{m}$ bands, ALMA and IRAM30m observed BL Lac at 1.3 mm during three scans at the end of the eastern subarray scheduling block of the 2018 October session. Those data were searched using the same HOPS incoherent averaging method as was used for the $870 \mu\text{m}$ observations and provide an independent application of the approach. The 1.3 mm scans provide a check of the $870 \mu\text{m}$ processing and a point of comparison for the $870 \mu\text{m}$ detections.

The amplitude and S/N values for one of the 1.3 mm scans are plotted in Figure 6 versus the duration of incoherently averaged segments. The S/N values are approximately tenfold greater at 1.3 mm than at $870 \mu\text{m}$ (see Figure 3), which likely results from a combination of factors that boost sensitivity at the longer wavelength: lower opacity, lower receiver noise, greater aperture efficiency, a wider beam, greater coherence, and greater source flux density. The coherence time determined using HOPS was comparable for the three scans to what was found at $870 \mu\text{m}$: on the order of 6–30 s. As with the $870 \mu\text{m}$ measurements, the S/N values asymptote as the segment duration decreases below the coherence time. The consistency of the S/N trends in the $870 \mu\text{m}$ and 1.3 mm scans suggests that the behavior is a real feature of the data and not an artifact of the analysis.

Comparison of the 1.3 mm and $870 \mu\text{m}$ wavelengths observing BL Lac also shows that the latter is a much more difficult regime in which to operate. The atmospheric conditions at the IRAM30m site (see Figure 1; $\tau_{345} \sim 0.8$) were not ideal for $870 \mu\text{m}$ observing during the test. At 1.3 mm, strong detections were obtained on all polarizations for each of the three attempted scans. At $870 \mu\text{m}$, detections were made on just two of four polarizations for a single ALMA–IRAM30m scan, and none were made on other BL Lac baselines. The tenfold greater S/N values at 1.3 mm are consistent with the system equivalent flux density (SEFD). The SEFDs on BL Lac scans at ALMA were approximately 150 Jy at 1.3 mm versus 580 Jy at $870 \mu\text{m}$ (a factor of 3.9 change). At IRAM30m, SEFDs during the BL Lac scans were 3800 Jy at 1.3 mm versus 10^5 Jy at $870 \mu\text{m}$ (a factor of approximately 25 change). The S/N is inversely proportional to the root product of the SEFDs, or $\sqrt{3.9 \times 25} \approx 10$, which explains the behavior across observing wavelengths. The significantly greater noise at $870 \mu\text{m}$ as well as the other losses associated with narrower beamwidth or coherence is the likely reason for nondetections to some stations and on certain scans.

Fringe power contours at 1.3 mm are plotted as a function of multiband delay and rate in Figure 7, exhibiting obvious peaks. The delays for each of the four polarization cross products is consistent across scans, and the 1.3 mm fringes are summarized in Table 2. All four polarization cross-hands are detected in each of the three 1.3 mm scans. The $6.4 \text{ G}\lambda$ spatial frequencies are 50% smaller than the $870 \mu\text{m}$ scans on the AP baseline, which corresponds to the frequency scaling between the two bands. The 1.3 mm zero-baseline flux density of BL Lac deduced from the ALMA local interferometry (Crew et al. 2023) was 1.2 Jy.

3.3. Coherence and Allan Deviation

It is convenient to characterize the phase noise of an interferometer by its Allan deviation, which is a measure of

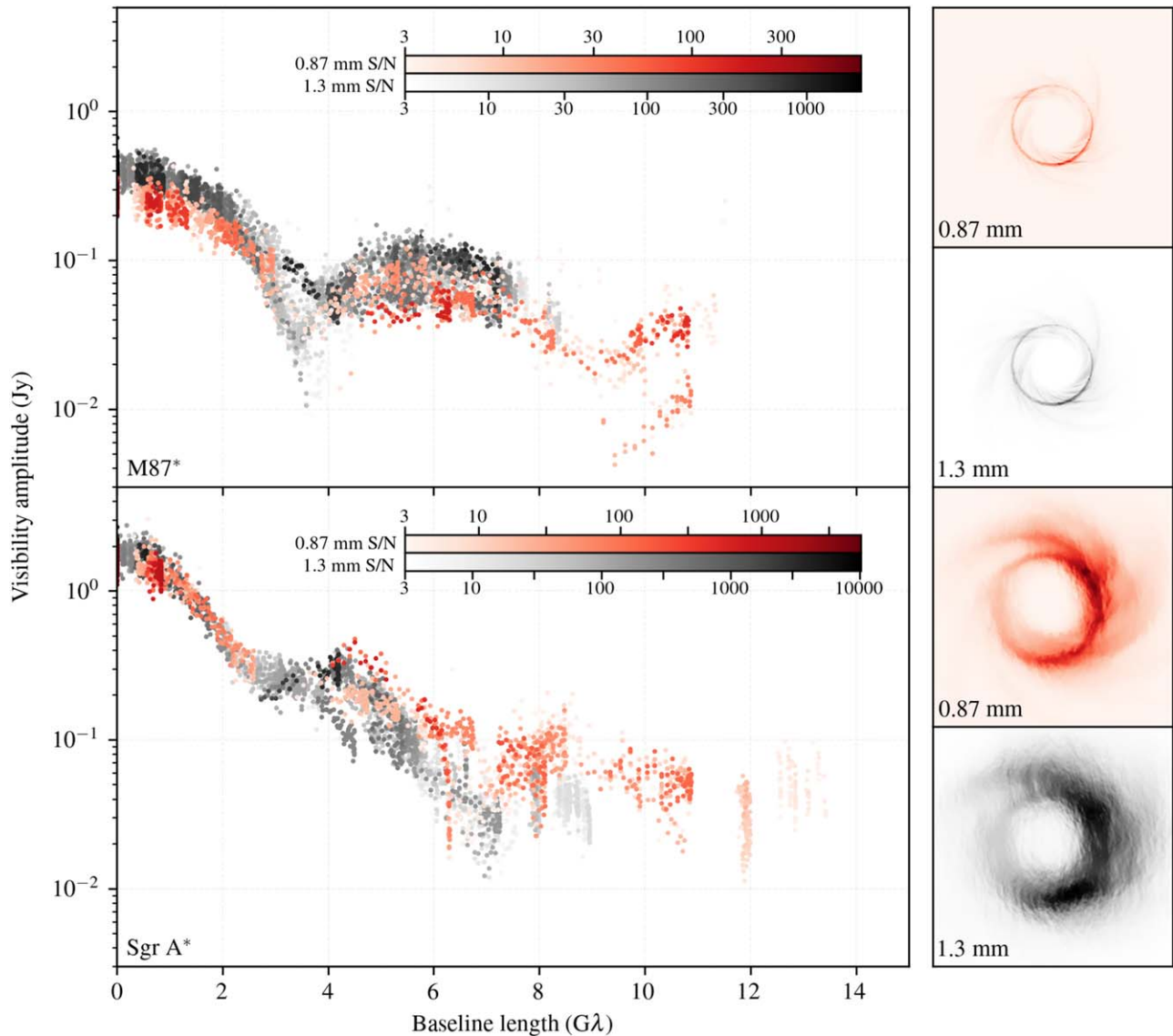


Figure 9. Left: visibility amplitudes for simulated observations of M87* (top) and Sgr A* (bottom) at observing wavelengths of 1.3 mm (gray) and 0.87 mm (red). The synthetic data have been generated using the `ngehtsim` package assuming array specifications appropriate for the phase 2 ngEHT array from Doeleman et al. (2023), including simultaneous dual-band observations, the use of the FPT calibration technique, and 16 GHz of bandwidth at both frequencies. Data points are colored by their S/N on an integration time of 5 minutes, and data points with $S/N < 3$ have been flagged. Right: images produced from GRMHD simulations of the M87* (top two panels; Event Horizon Telescope Collaboration et al. 2019e) and Sgr A* (bottom two panels; Event Horizon Telescope Collaboration et al. 2022b) accretion flows, used to generate the synthetic data shown in the left panels. Both simulations have been ray-traced at observing wavelengths of 1.3 mm (gray) and 0.87 mm (red), and the frequency-dependent effects of interstellar scattering have been applied to the Sgr A* images (Johnson 2016; Johnson et al. 2018).

fractional stability for an oscillator, time standard, or any time-variable process. When computing the Allan deviation of an observed VLBI interferometer phase, one normalizes by the frequency of observation to produce a dimensionless quantity. The relationships of Allan deviation to the statistical variance, coherence, and phase power spectrum can be found in Thompson et al. (2017). Examples of the Allan deviation of VLBI systems referenced to hydrogen maser time standards and operating at 1.3 cm and 3 mm wavelengths can be found in Rogers & Moran (1981) and Rogers et al. (1984), respectively, and show that at short wavelengths, decoherence is a potential concern. Alternatives to hydrogen masers for short-wavelength VLBI work have been explored (e.g., Doeleman et al. 2011). In this section, we compare the observed Allan deviation of the VLBI interferometric phase to limiting factors including the stability of time and frequency standards used in the

experiment as well as instabilities due to atmospheric turbulence.

Figure 8 shows the Allan deviation for $870 \mu\text{m}$ scans on the ALMA–SMA baseline. Over most integration times, the $870 \mu\text{m}$ Allan deviation is comparable to but greater than the maser–maser reference. The $870 \mu\text{m}$ traces exhibit relatively small scan-to-scan variation during the course of the brief fringe test when conditions were relatively stable. For comparison, Figure 8 also shows the Allan deviations for a large number of high-S/N 1.3 mm scans from the 2017 EHT campaign (Event Horizon Telescope Collaboration et al. 2019d). At times of less than about 5 s, the red 1.3 mm traces all approach the limit set by the maser references. At times longer than 5 s, the red traces are noticeably scattered. The scatter exists because of the variability of atmospheric conditions during the course of an observing campaign.

The tropospheric delay is essentially independent of wavelength for wavelengths longer than about $600\ \mu\text{m}$ as described by the Smith–Weintraub equation (see Thompson et al. 2017, Chapter 13). Thus, the Allan deviation is expected to be independent of wavelength for our observations. When the atmospheric conditions are stable, the 1.3 mm Allan deviation for individual scans approaches the maser–maser limit across all integration times. The mean of the 1.3 mm scans is within a factor of approximately 2 of the mean of the $870\ \mu\text{m}$ traces. The $870\ \mu\text{m}$ mean Allan deviation on the plot happens to be lower than the 1.3 mm mean for most integration times. However, we do not consider this difference to be significant given the extremely small $870\ \mu\text{m}$ data set. Further, the observations in 2017 April and 2018 October were of course made in differing weather conditions.

To assess the impact of atmospheric turbulence at longer times, the Allan deviation associated with atmospheric Kolmogorov turbulence is plotted for a set of nominal conditions following the approach outlined by Treuhaft & Lanyi (1987): $10\ \text{m s}^{-1}$ wind speed, 2 km troposphere scale height, $1.99 \times 10^{-7}\ \text{m}^{-1/3}$ Kolmogorov coefficient, and independent distant sites. The nominal Kolmogorov trace exceeds the maser–maser Allan deviation at longer times, where we expect atmospheric effects to dominate. Beyond 10 s, the nominal Kolmogorov trace matches the shape of the 1.3 mm mean. Although the $870\ \mu\text{m}$ mean falls somewhere between the maser–maser and nominal Kolmogorov limits, the atmospheric contribution may become more apparent in the future with scans spanning more variable weather conditions.

3.4. Phasing Efficiency

An important figure of merit when used to monitor the performance of phased array beamformers is phasing efficiency. This is a measure of how effectively outputs of the dishes in the local array are coherently summed to synthesize a single IF output from the array’s aggregated collecting area. For each array site, periodic estimates of phasing efficiency over time are stored with other essential metadata for use in calibration.

The ALMA and SMA phased arrays experienced lower and more variable phasing efficiency during the $870\ \mu\text{m}$ test than is typical for 1.3 mm observing in similar conditions. At $870\ \mu\text{m}$, atmospheric opacity is between 3 and 3.5 times that for 1.3 mm given the same precipitable water vapor. Further source fluxes decline with increasing frequency or shorter wavelength. Both of these factors result in a lower local array fringe S/N. There is thus greater error in the fits of the antenna phase corrections. Tuning within the band avoids the deep absorption lines due to atmospheric water resonances at 325 and 385 GHz, which would reduce the S/N still further. Also, the atmospheric phase fluctuations tracked by the adaptive phased array system have a greater amplitude for observations in the higher-frequency band. Crew et al. (2023) note that that moist, windy conditions tend to diminish phasing efficiency, and the winds were quite high at ALMA during the test. At dry, less windy times, ALMA obtained higher phasing efficiencies approaching 100%. While NOEMA participated in this test with a single dish, not as a phased array, all of these factors are expected to apply as well to NOEMA, which is now equipped with a phased array backend capable of beamforming in both the 1.3 mm and $870\ \mu\text{m}$ bands.

Water vapor radiometer (WVR) based phasing corrections were not in use during the 2018 test. Independent testing at ALMA shows that fast WVR corrections are effective at improving the efficiency when phase fluctuations are primarily due to water vapor. Phasing control loop algorithms are constantly being improved and in future will be better tuned to the $870\ \mu\text{m}$ wave band. These improvements will expand the opportunities for $870\ \mu\text{m}$ observing in a wider range of weather conditions and on weaker sources. Despite these challenges, VLBI detections at $870\ \mu\text{m}$ can be readily achieved even when phasing efficiencies are relatively low and in nonideal weather conditions.

4. Future Directions

Achieving $870\ \mu\text{m}$ VLBI fringes has strong implications for science directions that future global arrays operating at this wavelength can explore. As angular resolution scales with wavelength, we anticipate improving resolution from ~ 23 to $\sim 15\ \mu\text{as}$ on the longest EHT baselines (Figure 5). Plasma propagation processes typically scale as wavelength squared, so at $870\ \mu\text{m}$, scatter broadening of Sgr A* reduces to $\sim 5\ \mu\text{as}$, further sharpening resolution and increasing signal-to-noise on the longest VLBI baselines. Similarly, Faraday rotation measured across the bandpass of EHT receivers at $870\ \mu\text{m}$ can be used to improve estimates of accretion plasma densities and magnetic field geometries close to EHT targets. For both Sgr A* and M87*, the images at $870\ \mu\text{m}$ and 1.3 mm are determined predominantly by the achromatic gravitational lensing and hence should exhibit similar characteristics, implying that the aggregate Fourier coverage of VLBI observations at different frequencies can be used to improve modeling of the gravitationally lensed emission and the imaging fidelity generally (Chael et al. 2023). Figure 9 shows Fourier amplitudes as a function of radius for GRMHD¹⁵⁶ models of M87* and Sgr A*. Inclusion of 345 GHz observations adds coverage in the visibility plane regions not sampled at 230 GHz, and it extends baseline lengths for higher angular resolution as well as enhanced overall sampling of Fourier spatial frequencies to allow dynamical reconstructions of accretion and jet launch close to the event horizon.

There are several developments that will increase the sensitivity and flexibility of $870\ \mu\text{m}$ VLBI in the near future. Next-generation VLBI backends (Doeleman et al. 2023) will allow an increase in data capture rates from 64 to $128\ \text{Gb s}^{-1}$ (per observing frequency band), lowering detection thresholds by $\sqrt{2}$. Additional use of the frequency phase transfer (FPT) technique (Rioja et al. 2023) through simultaneous observations at 86, 230, and 345 GHz will extend coherent integration times at higher frequencies, further increasing sensitivity. In optimal cases, this increase will be the square root of the ratio of coherence times at 86 GHz and 345 GHz ($\sqrt{\tau_c(86)/\tau_c(345)}$). And the participation of more telescopes at high-altitude sites will make the EHT array more robust against adverse weather conditions, increasing the opportunities for staging $870\ \mu\text{m}$ VLBI observations (Raymond et al. 2021; Doeleman et al. 2023). Anticipated upgrades to ALMA will be exceptionally useful to advance $870\ \mu\text{m}$ VLBI and are planned on a similar timeline (~ 2030) as the ngEHT upgrade (Carpenter et al. 2023). In particular, the projected doubling of the continuum bandwidth of ALMA will match the ngEHT specifications, and

¹⁵⁶ General relativistic magnetohydrodynamic.

a subarray capability at ALMA will enable simultaneous multiband observations that benefit from FPT as noted above. In sum, the prospects for routine 870 μm VLBI in the near future are excellent.

5. Conclusions

VLBI fringe detections on baselines between ALMA–APEX, ALMA–IRAM30m, and ALMA–SMA have been achieved at 870 μm for multiple AGN sources. S/Ns were between approximately 10 and 70. Despite marginal weather conditions across the array, detections to multiple stations and sources were obtained. This work demonstrates that the EHT instrumentation is viable at 870 μm (345 GHz) and will provide a critical advance in array capability. EHT-wide observations at 870 μm would yield a fringe spacing of about 15 μas and, with a full track of coverage, would significantly enhance the fine details of the EHT images of AGN and horizon-scale targets (Doeleman et al. 2019, 2023; Johnson et al. 2023).

Acknowledgments

This work was supported by the National Science Foundation (grants AST-1935980, AST-1743747, AST-1440254), an ALMA Cycle 5 North America Development Award, the Gordon and Betty Moore Foundation (awards GBMF3561, GBMF5278, and GBMF10423), and a generous gift from the Deepak Raghavan Family Foundation. Work on this project was conducted in part at the Black Hole Initiative at Harvard University (funded through grants 60477, 61479, and 62286 from the John Templeton Foundation and grant GBMF8273 from the Gordon and Betty Moore Foundation). This work is partly based on observations carried out with the IRAM 30 m telescope and the NOEMA Interferometer. IRAM is supported by INSU/CNRS (France), MPG (Germany), and IGN (Spain). The IRAM NOEMA phasing project was supported by the European Research Council (ERC) Synergy Grant “Black-HoleCam: Imaging the Event Horizon of Black Holes” (grant 610058). The Submillimeter Array is a joint project between the Smithsonian Astrophysical Observatory and the Academia Sinica Institute of Astronomy and Astrophysics and is funded by the Smithsonian Institution and the Academia Sinica. The SMA gratefully acknowledges the efforts of its staff for supporting these observations, including those of the operator on duty, R. Howie. This publication is based on data acquired with the APEX. APEX is a collaboration between the Max-Planck-Institut für Radioastronomie, the European Southern Observatory, and the Onsala Space Observatory. This work was an activity external to JPL, and effort by A.R. was not in their capacity as an employee of the Jet Propulsion Laboratory, California Institute of Technology. The GLT is supported by the the Ministry of Science and Technology (MOST) of Taiwan (103-2119-M-001-010-MY2, 105-2119-M-001-042, 106-2119-M-001-013, 107-2119-M-001-041, 108-2112-M-001-048, 109-2124-M-001-005, 110-2124-M-001-007) and the National Science and Technology Council (NSTC) of Taiwan (111-2124-M-001-005, 112-2124-M-001-014).

The Event Horizon Telescope Collaboration additionally thanks the following organizations and programs: the Academia Sinica; the Academy of Finland (projects 274477, 284495, 312496, 315721); the Agencia Nacional de Investigación y Desarrollo (ANID), Chile via NCN19₀₅₈ (TITANs), Fondecyt 1221421 and BASAL FB210003; the Alexander von Humboldt

Stiftung; an Alfred P. Sloan Research Fellowship; Allegro, the European ALMA Regional Centre node in the Netherlands, the NL astronomy research network NOVA, and the astronomy institutes of the University of Amsterdam, Leiden University, and Radboud University; the ALMA North America Development Fund; the Astrophysics and High Energy Physics program by MCIN (with funding from European Union NextGenerationEU, PRTR-C1711); the Brinson Foundation; “la Caixa” Foundation (ID 100010434) through fellowship codes LCF/BQ/DI22/11940027 and LCF/BQ/DI22/11940030; Chandra DD7-18089X and TM6-17006X; the China Scholarship Council; the China Postdoctoral Science Foundation fellowships (2020M671266, 2022M712084); Consejo Nacional de Humanidades, Ciencia y Tecnología (CON-AHCYT, Mexico, projects U0004-246083, U0004-259839, F0003-272050, M0037-279006, F0003-281692, 104497, 275201, 263356); the Colfuturo Scholarship; the Consejería de Economía, Conocimiento, Empresas y Universidad of the Junta de Andalucía (grant P18-FR-1769); the Consejo Superior de Investigaciones Científicas (grant 2019AEP112); the Delaney Family via the Delaney Family John A. Wheeler Chair at Perimeter Institute; Dirección General de Asuntos del Personal Académico-Universidad Nacional Autónoma de México (DGAPA-UNAM, projects IN112820 and IN108324); the Dutch Research Council (NWO) for the VICI award (grant 639.043.513), the grant OCENW.KLEIN.113, and the Dutch Black Hole Consortium (with project No. NWA 1292.19.202) of the research program the National Science Agenda; the Dutch National Supercomputers, Cartesius and Snellius (NWO grant 2021.013); the EACOA Fellowship awarded by the East Asia Core Observatories Association, which consists of the Academia Sinica Institute of Astronomy and Astrophysics, the National Astronomical Observatory of Japan, Center for Astronomical Mega-Science, Chinese Academy of Sciences, and the Korea Astronomy and Space Science Institute; the European Union Horizon 2020 research and innovation program under grant agreements RadioNet (No. 730562), M2FINDERS (No. 101018682), and FunFiCO (No. 777740); the European Research Council for the advanced grant “JETSET: Launching, propagation and emission of relativistic jets from binary mergers and across mass scales” (grant No. 884631); the European Horizon Europe staff exchange (SE) program HORIZON-MSCA-2021-SE-01 grant NewFunFiCO (No. 10108625); the Horizon ERC Grants 2021 program under grant agreement No. 101040021; the FAPESP (Fundação de Amparo à Pesquisa do Estado de São Paulo) under grant 2021/01183-8; the Fondo CAS-ANID folio CAS220010; the Generalitat Valenciana (grants APOSTD/2018/177 and ASFAE/2022/018) and GenT Program (project CIDEAGENT/2018/021); the Institute for Advanced Study; the Istituto Nazionale di Fisica Nucleare (INFN) sezione di Napoli, iniziative specifiche TEONGRAV; the International Max Planck Research School for Astronomy and Astrophysics at the Universities of Bonn and Cologne; DFG research grant “Jet physics on horizon scales and beyond” (grant No. 443220636); Joint Columbia/Flatiron Postdoctoral Fellowship (research at the Flatiron Institute is supported by the Simons Foundation); the Japan Ministry of Education, Culture, Sports, Science and Technology (MEXT; grant JPMXP1020200109); the Japan Society for the Promotion of Science (JSPS) Grant-in-Aid for JSPS Research Fellowship (JP17J08829); the Joint Institute for Computational Fundamental Science, Japan; the Key Research

Program of Frontier Sciences, Chinese Academy of Sciences (CAS; grants QYZDJ-SSW-SLH057, QYZDJSSW-SYS008, ZDBS-LY-SLH011); the Leverhulme Trust Early Career Research Fellowship; the Max-Planck-Gesellschaft (MPG); the Max Planck Partner Group of the MPG and the CAS; the MEXT/JSPS KAKENHI (grants 18KK0090, JP21H01137, JP18H03721, JP18K13594, 18K03709, JP19K14761, 18H01245, 25120007, 19H01943, 21H01137, 21H04488, 22H00157, 23K03453); the MICINN Research Projects PID2019-108995GB-C22, PID2022-140888NB-C22; the MIT International Science and Technology Initiatives (MISTI) Funds; the Ministry of Science and Technology (MOST) of Taiwan (105-2112-M-001-025-MY3, 106-2112-M-001-011, 106-2119-M-001-027, 106-2923-M-001-005, 107-2119-M-001-017, 107-2119-M-001-020, 107-2119-M-110-005, 107-2923-M-001-009, 108-2112-M-001-051, 108-2923-M-001-002, 109-2112-M-001-025, 109-2923-M-001-001, 110-2112-M-001-033, 110-2923-M-001-001, and 112-2112-M-003-010-MY3); the Ministry of Education (MoE) of Taiwan Yushan Young Scholar Program; the Physics Division, National Center for Theoretical Sciences of Taiwan; the National Aeronautics and Space Administration (NASA; Fermi Guest Investigator grant 80NSSC23K1508, NASA Astrophysics Theory Program grant 80NSSC20K0527, NASA NuSTAR award 80NSSC20K0645); NASA Hubble Fellowship grants HST-HF2-51431.001-A and HST-HF2-51482.001-A awarded by the Space Telescope Science Institute, which is operated by the Association of Universities for Research in Astronomy, Inc., for NASA, under contract NAS5-26555; the National Institute of Natural Sciences (NINS) of Japan; the National Key Research and Development Program of China (grants 2016YFA0400704, 2017YFA0402703, 2016YFA0400702); the National Science and Technology Council (NSTC; grants NSTC 111-2112-M-001-041, NSTC 111-2124-M-001-005, NSTC 112-2124-M-001-014); the US National Science Foundation (NSF; grants AST-0096454, AST-0352953, AST-0521233, AST-0705062, AST-0905844, AST-0922984, AST-1126433, OIA-1126433, AST-1140030, DGE-1144085, AST-1207704, AST-1207730, AST-1207752, MRI-1228509, OPP-1248097, AST-1310896, AST-1555365, AST-1614868, AST-1615796, AST-1715061, AST-1716327, AST-1726637, OISE-1743747, AST-1816420, AST-1952099, AST-2034306, AST-2205908, AST-2307887); NSF Astronomy and Astrophysics Postdoctoral Fellowship (AST-1903847); the Natural Science Foundation of China (grants 11650110427, 10625314, 11721303, 11725312, 11873028, 11933007, 11991052, 11991053, 12192220, 12192223, 12273022, 12325302, 12303021); the Natural Sciences and Engineering Research Council of Canada (NSERC; including a Discovery Grant and the NSERC Alexander Graham Bell Canada Graduate Scholarships-Doctoral Program); the National Research Foundation of Korea (the Global PhD Fellowship Grant: grants NRF-2015H1A2A1033752, the Korea Research Fellowship Program: NRF-2015H1D3A1066561, Brain Pool Program: 2019H1D3A1A01102564, Basic Research Support grant 2019R1F1A1059721, 2021R1A6A3A01086420, 2022R1C1C1005255, 2022R1F1A1075115); Netherlands Research School for Astronomy (NOVA) Virtual Institute of Accretion (VIA) postdoctoral fellowships; NOIRLab, which is managed by the Association of Universities for Research in Astronomy (AURA) under a cooperative agreement with the National Science Foundation; Onsala Space Observatory (OSO) national infrastructure for the provisioning of its facilities/observational support (OSO receives funding through the Swedish Research Council under grant 2017-00648); the Perimeter

Institute for Theoretical Physics (research at Perimeter Institute is supported by the Government of Canada through the Department of Innovation, Science and Economic Development and by the Province of Ontario through the Ministry of Research, Innovation and Science); the Portuguese Foundation for Science and Technology (FCT) grants (Individual CEEC program—5th edition, <https://doi.org/10.54499/UIDP/04106/2020>, PTDC/FIS-AST/3041/2020, CERN/FIS-PAR/0024/2021, 2022.04560.PTDC); the Princeton Gravity Initiative; the Spanish Ministerio de Ciencia e Innovación (grants PGC2018-098915-B-C21, AYA2016-80889-P, PID2019-108995GB-C21, PID2020-117404GB-C21); the University of Pretoria for financial aid in the provision of the new Cluster Server nodes and SuperMicro (USA) for a SEEDING GRANT approved toward these nodes in 2020; the Shanghai Municipality orientation program of basic research for international scientists (grant No. 22JC1410600); the Shanghai Pilot Program for Basic Research, Chinese Academy of Science, Shanghai Branch (JCYJ-SHFY-2021-013); the State Agency for Research of the Spanish MCIU through the “Center of Excellence Severo Ochoa” award for the Instituto de Astrofísica de Andalucía (SEV-2017-0709); the Spanish Ministry for Science and Innovation grant CEX2021-001131-S funded by MCIN/AEI/10.13039/501100011033; the Spinoza Prize SPI 78-409; the South African Research Chairs Initiative through the South African Radio Astronomy Observatory (SARAO; grant ID 77948), which is a facility of the National Research Foundation (NRF), an agency of the Department of Science and Innovation (DSI) of South Africa; the Swedish Research Council (VR); the Taplin Fellowship; the Toray Science Foundation; the UK Science and Technology Facilities Council (grant no. ST/X508329/1); the US Department of Energy (USDOE) through the Los Alamos National Laboratory (operated by Triad National Security, LLC, for the National Nuclear Security Administration of the USDOE, contract 89233218CNA000001); and the YCAA Prize Postdoctoral Fellowship.

We thank the staff at the participating observatories, correlation centers, and institutions for their enthusiastic support. This paper makes use of the following ALMA data: ADS/JAO.ALMA#2016.1.01154.V, ADS/JAO.ALMA#2011.0.00010.E, and ADS/JAO.ALMA#2011.0.00012.E. See <https://almascience.nrao.edu/alma-data/eht-2018> for more detail and access to the data. ALMA is a partnership of the European Southern Observatory (ESO; Europe, representing its member states), NSF, and National Institutes of Natural Sciences of Japan, together with National Research Council (Canada), Ministry of Science and Technology (MOST; Taiwan), Academia Sinica Institute of Astronomy and Astrophysics (ASIAA; Taiwan), and Korea Astronomy and Space Science Institute (KASI; Republic of Korea), in cooperation with the Republic of Chile. The Joint ALMA Observatory is operated by ESO, Associated Universities, Inc. (AUI)/NRAO, and the National Astronomical Observatory of Japan (NAOJ). The NRAO is a facility of the NSF operated under cooperative agreement by AUI. This research used resources of the Oak Ridge Leadership Computing Facility at the Oak Ridge National Laboratory, which is supported by the Office of Science of the U.S. Department of Energy under contract No. DE-AC05-00OR22725; the ASTROVIVES FEDER infrastructure, with project code IDIFEDER-2021-086; and the computing cluster of the Shanghai VLBI correlator supported by the Special Fund for Astronomy from the Ministry of Finance in China. We also thank the Center for Computational Astrophysics, National Astronomical Observatory of Japan. This work was

Georgios Filippou Paraschos  <https://orcid.org/0000-0001-6757-3098>
 Jongho Park  <https://orcid.org/0000-0001-6558-9053>
 Harriet Parsons  <https://orcid.org/0000-0002-6327-3423>
 Ue-Li Pen  <https://orcid.org/0000-0003-2155-9578>
 Vincent Piétu  <https://orcid.org/0009-0006-3497-397X>
 Oliver Porth  <https://orcid.org/0000-0002-4584-2557>
 Ben Prather  <https://orcid.org/0000-0002-0393-7734>
 Giacomo Principe  <https://orcid.org/0000-0003-0406-7387>
 Dimitrios Psaltis  <https://orcid.org/0000-0003-1035-3240>
 Hung-Yi Pu  <https://orcid.org/0000-0001-9270-8812>
 Ramprasad Rao  <https://orcid.org/0000-0002-1407-7944>
 Mark G. Rawlings  <https://orcid.org/0000-0002-6529-202X>
 Angelo Ricarte  <https://orcid.org/0000-0001-5287-0452>
 Bart Ripperda  <https://orcid.org/0000-0002-7301-3908>
 Freek Roelofs  <https://orcid.org/0000-0001-5461-3687>
 Cristina Romero-Cañizales  <https://orcid.org/0000-0001-6301-9073>
 Eduardo Ros  <https://orcid.org/0000-0001-9503-4892>
 Arash Roshanineshat  <https://orcid.org/0000-0002-8280-9238>
 Ignacio Ruiz  <https://orcid.org/0000-0002-0965-5463>
 Chet Ruszczyk  <https://orcid.org/0000-0001-7278-9707>
 Kazi L. J. Rygl  <https://orcid.org/0000-0003-4146-9043>
 David Sánchez-Argüelles  <https://orcid.org/0000-0002-7344-9920>
 Miguel Sánchez-Portal  <https://orcid.org/0000-0003-0981-9664>
 Mahito Sasada  <https://orcid.org/0000-0001-5946-9960>
 Kaushik Satapathy  <https://orcid.org/0000-0003-0433-3585>
 Tuomas Savolainen  <https://orcid.org/0000-0001-6214-1085>
 Jonathan Schonfeld  <https://orcid.org/0000-0002-8909-2401>
 Karl-Friedrich Schuster  <https://orcid.org/0000-0003-2890-9454>
 Lijing Shao  <https://orcid.org/0000-0002-1334-8853>
 Zhiqiang Shen (沈志强)  <https://orcid.org/0000-0003-3540-8746>
 Des Small  <https://orcid.org/0000-0003-3723-5404>
 Bong Won Sohn  <https://orcid.org/0000-0002-4148-8378>
 Jason SooHoo  <https://orcid.org/0000-0003-1938-0720>
 León David Sosapanta Salas  <https://orcid.org/0000-0003-1979-6363>
 Kamal Souccar  <https://orcid.org/0000-0001-7915-5272>
 Joshua S. Stanway  <https://orcid.org/0009-0003-7659-4642>
 He Sun (孙赫)  <https://orcid.org/0000-0003-1526-6787>
 Fumie Tazaki  <https://orcid.org/0000-0003-0236-0600>
 Alexandra J. Tetarenko  <https://orcid.org/0000-0003-3906-4354>
 Paul Tiede  <https://orcid.org/0000-0003-3826-5648>
 Kenji Toma  <https://orcid.org/0000-0002-7114-6010>
 Teresa Toscano  <https://orcid.org/0000-0003-3658-7862>
 Efthalia Traianou  <https://orcid.org/0000-0002-1209-6500>
 Sascha Trippe  <https://orcid.org/0000-0003-0465-1559>
 Matthew Turk  <https://orcid.org/0000-0002-5294-0198>
 Ilse van Bemmel  <https://orcid.org/0000-0001-5473-2950>
 Huib Jan van Langevelde  <https://orcid.org/0000-0002-0230-5946>
 Daniel R. van Rossum  <https://orcid.org/0000-0001-7772-6131>
 Jesse Vos  <https://orcid.org/0000-0003-3349-7394>
 Derek Ward-Thompson  <https://orcid.org/0000-0003-1140-2761>

John Wardle  <https://orcid.org/0000-0002-8960-2942>
 Jasmin E. Washington  <https://orcid.org/0000-0002-7046-0470>
 Robert Wharton  <https://orcid.org/0000-0002-7416-5209>
 Kaj Wiik  <https://orcid.org/0000-0002-0862-3398>
 Gunther Witzel  <https://orcid.org/0000-0003-2618-797X>
 Michael F. Wondrak  <https://orcid.org/0000-0002-6894-1072>
 George N. Wong  <https://orcid.org/0000-0001-6952-2147>
 Qingwen Wu (吴庆文)  <https://orcid.org/0000-0003-4773-4987>
 Nitika Yadlapalli  <https://orcid.org/0000-0003-3255-4617>
 Paul Yamaguchi  <https://orcid.org/0000-0002-6017-8199>
 Aristomenis Yfantis  <https://orcid.org/0000-0002-3244-7072>
 Doosoo Yoon  <https://orcid.org/0000-0001-8694-8166>
 Ziri Younsi  <https://orcid.org/0000-0001-9283-1191>
 Wei Yu (于威)  <https://orcid.org/0000-0002-5168-6052>
 Feng Yuan (袁峰)  <https://orcid.org/0000-0003-3564-6437>
 Ye-Fei Yuan (袁业飞)  <https://orcid.org/0000-0002-7330-4756>
 J. Anton Zensus  <https://orcid.org/0000-0001-7470-3321>
 Shuo Zhang  <https://orcid.org/0000-0002-2967-790X>
 Guang-Yao Zhao  <https://orcid.org/0000-0002-4417-1659>
 Shan-Shan Zhao (赵彬彬)  <https://orcid.org/0000-0002-9774-3606>

References

- Baath, L. B., Padin, S., Woody, D., et al. 1991, *A&A*, **241**, L1
 Baath, L. B., Rogers, A. E. E., Inoue, M., et al. 1992, *A&A*, **257**, 31
 Belitsky, V., Lapkin, I., Fredrixon, M., et al. 2018, *A&A*, **612**, A23
 Blackburn, L., Chan, C.-k., Crew, G. B., et al. 2019, *ApJ*, **882**, 23
 Carpenter, J., Brogan, C., Iono, D., & Mroczkowski, T. 2023, *Physics and Chemistry of Star Formation: The Dynamical ISM Across Time and Spatial Scales* (Köln: Universitäts- und Stadtbibliothek), 304
 Carter, M., Lazareff, B., Maier, D., et al. 2012, *A&A*, **538**, A89
 Chael, A., Issaoun, S., Pesce, D. W., et al. 2023, *ApJ*, **945**, 40
 Chen, M.-T., Asada, K., Matsushita, S., et al. 2023, *PASP*, **135**, 095001
 Chenu, J. Y., Carter, M., Maier, D., et al. 2007, in 2007 Joint 32nd Int. Conf. on Infrared and Millimeter Waves and the 15th Int. Conf. on Terahertz Electronics (New York: Curran Associates, Inc.), 176
 Chenu, J.-Y., Navarrini, A., Bortolotti, Y., et al. 2016, *ITST*, **6**, 223
 Crew, G. B., Goddi, C., Matthews, L. D., et al. 2023, *PASP*, **135**, 025002
 Deller, A. T., Brisken, W. F., Phillips, C. J., et al. 2011, *PASP*, **123**, 275
 Doleman, S., Blackburn, L., Dexter, J., et al. 2019, *BAAS*, **51**, 256
 Doleman, S., Mai, T., Rogers, A. E. E., et al. 2011, *PASP*, **123**, 582
 Doleman, S. S., Barrett, J., Blackburn, L., et al. 2023, *Galax*, **11**, 107
 Doleman, S. S., Fish, V. L., Schenck, D. E., et al. 2012, *Sci*, **338**, 355
 Doleman, S. S., Phillips, R. B., Rogers, A. E. E., et al. 2002, in Proc. of the 6th EVN Symp. (Bonn: Max-Planck-Institut für Radioastronomie), 223
 Doleman, S. S., Weintraub, J., Rogers, A. E. E., et al. 2008, *Natur*, **455**, 78
 Event Horizon Telescope Collaboration, Akiyama, K., Alberdi, A., et al. 2019a, *ApJL*, **875**, L1
 Event Horizon Telescope Collaboration, Akiyama, K., Alberdi, A., et al. 2019b, *ApJL*, **875**, L2
 Event Horizon Telescope Collaboration, Akiyama, K., Alberdi, A., et al. 2019c, *ApJL*, **875**, L4
 Event Horizon Telescope Collaboration, Akiyama, K., Alberdi, A., et al. 2019d, *ApJL*, **875**, L3
 Event Horizon Telescope Collaboration, Akiyama, K., Alberdi, A., et al. 2019e, *ApJL*, **875**, L5
 Event Horizon Telescope Collaboration, Akiyama, K., Alberdi, A., et al. 2022a, *ApJL*, **930**, L12
 Event Horizon Telescope Collaboration, Akiyama, K., Alberdi, A., et al. 2022b, *ApJL*, **930**, L16
 Event Horizon Telescope Collaboration, Akiyama, K., Alberdi, A., et al. 2024, *A&A*, **681**, A79

- Event Horizon Telescope Collaboration, Akiyama, K., Algaba, J. C., et al. 2021, *ApJL*, **910**, L13
- Goddi, C., Martí-Vidal, I., Messias, H., et al. 2019, *PASP*, **131**, 075003
- Greve, A., & Bremer, M. 2010, *Thermal Design and Thermal Behaviour of Radio Telescopes and their Enclosures* (Berlin: Springer), 364
- Greve, A., Könönen, P., Graham, D. A., et al. 2002, *A&A*, **390**, L19
- Greve, A., Torres, M., Wink, J. E., et al. 1995, *A&A*, **299**, L33
- Hada, K., Doi, A., Kino, M., et al. 2011, *Natur*, **477**, 185
- Han, C.-C., Chen, M.-T., Huang, Y.-D., et al. 2018, *Proc. SPIE*, **10708**, 1070835
- Inoue, M., Algaba-Marcos, J. C., Asada, K., et al. 2014, *RaSc*, **49**, 564
- Issaoun, S., Johnson, M. D., Blackburn, L., et al. 2019, *ApJ*, **871**, 30
- Issaoun, S., Wielgus, M., Jorstad, S., et al. 2022, *ApJ*, **934**, 145
- Janssen, M., Falcke, H., Kadler, M., et al. 2021, *NatAs*, **5**, 1017
- Janssen, M., Goddi, C., van Bemmell, I. M., et al. 2019, *A&A*, **626**, A75
- Johnson, M. D. 2016, *ApJ*, **833**, 74
- Johnson, M. D., Akiyama, K., Blackburn, L., et al. 2023, *Galax*, **11**, 61
- Johnson, M. D., Lupsasca, A., Strominger, A., et al. 2020, *SciA*, **6**, eaaz1310
- Johnson, M. D., Narayan, R., Psaltis, D., et al. 2018, *ApJ*, **865**, 104
- Jorstad, S., Wielgus, M., Lico, R., et al. 2023, *ApJ*, **943**, 170
- Kerr, A. R., Pan, S.-K., Claude, S. M. X., et al. 2014, *ITTST*, **4**, 201
- Kim, J.-y., Krichbaum, T. P., Broderick, A. E., et al. 2020, *A&A*, **640**, A69
- Klein, T., Ciechanowicz, M., Leinz, C., et al. 2014, *ITTST*, **4**, 588
- Koay, J. Y., Matsushita, S., Asada, K., et al. 2020, *Proc. SPIE*, **11445**, 114450Q
- Krichbaum, T. P., Graham, D. A., Alef, W., et al. 2002, in *Proc. of the 6th EVN Symp.*, ed. E. Ros et al. (Bonn: Max-Planck-Institut für Radioastronomie), 125
- Krichbaum, T. P., Graham, D. A., Greve, A., et al. 1997, *A&A*, **323**, L17
- Krichbaum, T. P., Graham, D. A., Witzel, A., et al. 1998, *A&A*, **335**, L106
- Levy, R., Antennas, I., & Society, P. 1996, *Structural Engineering of Microwave Antennas: For Electrical, Mechanical, and Civil Engineering* (New York: IEEE), https://books.google.com/books?id=qPV_QgAACAAJ
- Liebe, H. J. 1985, *RaSc*, **20**, 1069
- Lo, W.-P., Asada, K., Matsushita, S., et al. 2023, *ApJ*, **950**, 10
- Lobanov, A. P. 1998, *A&A*, **330**, 79
- Mahieu, S., Maier, D., Lazareff, B., et al. 2012, *ITTST*, **2**, 29
- Maier, D., Barbier, A., Lazareff, B., & Schuster, K. F. 2005, in *16th Int. Symp. on Space Terahertz Technology* (Göteborg: Chalmers Univ. Technology), 428
- Maier, D., Reverdy, J., Billon-Pierron, D., & Barbier, A. 2012, *ITTST*, **2**, 215
- Mangum, J. G., Baars, J. W. M., Greve, A., et al. 2006, *PASP*, **118**, 1257
- Martí-Vidal, I., Roy, A., Conway, J., & Zensus, A. J. 2016, *A&A*, **587**, A143
- Matsushita, S., Asada, K., Inoue, M., et al. 2018, *Proc. SPIE*, **10700**, 1070029
- Matsushita, S., Asada, K., Martin-Cocher, P. L., et al. 2016, *PASP*, **129**, 025001
- Matsushita, S., Martin-Cocher, P. L., Paine, S. N., et al. 2022, *PASP*, **134**, 125002
- Matsushita, S., Matsuo, H., Pardo, J. R., & Radford, S. J. E. 1999, *PASJ*, **51**, 603
- Mathews, L. D., Crew, G. B., Doeleman, S. S., et al. 2018, *PASP*, **130**, 015002
- Meledin, D., Lapkin, I., Fredrixon, M., et al. 2022, *A&A*, **668**, A2
- Okino, H., Akiyama, K., Asada, K., et al. 2022, *ApJ*, **940**, 65
- Padin, S., Woody, D. P., Hodges, M. W., et al. 1990, *ApJL*, **360**, L11
- Paine, S. 2022, *The am atmospheric model*, Zenodo, doi:10.5281/zenodo.6774378
- Palumbo, D. C. M., Wong, G. N., Chael, A., & Johnson, M. D. 2023, *ApJL*, **952**, L31
- Paraschos, G. F., Kim, J. Y., Wielgus, M., et al. 2024, *A&A*, **682**, L3
- Pesce, D. W., Palumbo, D. C. M., Narayan, R., et al. 2021, *ApJ*, **923**, 260
- Primiani, R. A., Young, K. H., Young, A., et al. 2016, *JAI*, **5**, 1641006
- Raffin, P., Ho, P. T. P., Asada, K., et al. 2016, *Proc. SPIE*, **9906**, 99060U
- Ramakrishnan, V., Nagar, N., Arratia, V., et al. 2023, *Galax*, **11**, 15
- Raymond, A. W., Palumbo, D., Paine, S. N., et al. 2021, *ApJS*, **253**, 5
- Readhead, A. C. S., Mason, C. R., Mofett, A. T., et al. 1983, *Natur*, **303**, 504
- Rioja, M. J., Dodson, R., & Asaki, Y. 2023, *Galax*, **11**, 16
- Rogers, A. E., & Moran, J. M. 1981, *ITIM*, **30**, 283
- Rogers, A. E. E., Doeleman, S. S., & Moran, J. M. 1995, *AJ*, **109**, 1391
- Rogers, A. E. E., Moffet, A. T., Backer, D. C., & Moran, J. M. 1984, *RaSc*, **19**, 1552
- Thompson, A. R., Moran, J. M., & Swenson, G. W., Jr 2017, *Interferometry and Synthesis in Radio Astronomy* (3rd ed.; Berlin: Springer)
- Tong, C. Y. E., Blundell, R., Megerian, K. G., et al. 2005, *ITAS*, **15**, 490
- Tong, C.-Y. E., Grimes, P., Blundell, R., Wang, M.-J., & Noguchi, T. 2013, *ITTST*, **3**, 428
- Treuhaft, R. N., & Lanyi, G. E. 1987, *RaSc*, **22**, 251
- Tuccari, G., Alef, W., Wunderlich, M., et al. 2017, in *23rd European VLBI Group for Geodesy and Astrometry Working Meeting*, ed. R. Haas & G. Elgered Gothenburg (EGA), 78
- Vertatschitsch, L., Primiani, R., Young, A., et al. 2015, *PASP*, **127**, 1226
- Whitney, A. R., Cappallo, R., Aldrich, W., et al. 2004, *RaSc*, **39**, RS1007
- Wielgus, M., Issaoun, S., Martí-Vidal, I., et al. 2024, *A&A*, **682**, A97
- Young, A., Primiani, R., Weintroub, J., et al. 2016, in *2016 IEEE Int. Symp. on Phased Array Systems and Technology (PAST)* (New York: IEEE), 1
- Zhao, G.-Y., Gómez, J. L., Fuentes, A., et al. 2022, *ApJ*, **932**, 72